Measurement Accuracy of Inspiraling Eccentric Neutron Star and Black Hole Binaries Using Gravitational Waves

László Gondán and Bence Kocsis
Eötvös University, Institute of Physics, Pázmány P. s. 1/A, Budapest, 1117, Hungary
Received 2018 August 20; revised 2018 December 5; accepted 2018 December 14; published 2019 January 30

Abstract

In a recent paper, we determined the measurement accuracy of physical parameters for eccentric, precessing, non-spinning, inspiraling, stellar-mass black hole - black hole (BH–BH) binaries for the upcoming second-generation LIGO/VIRGO/KAGRA detector network at design sensitivity using the Fisher matrix method. Here we extend that study to a wide range of binary masses including neutron star - neutron star (NS–NS), NS–BH, and BH–BH binaries with BH masses up to 110 $M_\odot$. The measurement error of eccentricity $e_{10\,\mathrm{Hz}}$ at a gravitational-wave (GW) frequency of 10 Hz is in the range $(10^{-4} - 10^{-3}) \times (D_L/100\,\mathrm{Mpc})$ for NS–NS, NS–BH, and BH–BH binaries at a luminosity distance of D_L if $e_{10\,\mathrm{Hz}} \gtrsim 0.1$. For events with masses and distances similar to the detected 10 GW transients, we show that nonzero orbital eccentricities may be detected if $0.081 \lesssim e_{10\,\mathrm{Hz}}$. Consequently, the LIGO/VIRGO/KAGRA detector network at design sensitivity will have the capability to distinguish between eccentric waveforms and circular waveforms. In comparison to circular inspirals, we find that the chirp mass measurement precision can improve by up to a factor of ~20 and ~50–100 for NS–NS and NS–BH binaries with BH companion masses $\lesssim 40$ $M_\odot$, respectively. The identification of eccentric sources may give information on their astrophysical origin; it would indicate merging binaries in triple or higher multiplicity systems or dynamically formed binaries in dense stellar systems such as globular clusters or galactic nuclei.

Key words: black hole physics – gravitational waves – stars: neutron

1. Introduction

The Advanced Laser Interferometer Gravitational-wave Observatory[1] (aLIGO) detectors (Aasi et al. 2015) and Advanced Virgo[2] (AdV, Acernese et al. 2015) have made the first 10 detections of gravitational waves (GWs) during the first and second observing runs (Abbott et al. 2016b, 2016c, 2017a, 2017b, 2017c, 2017d; The LIGO Scientific Collaboration & the Virgo Collaboration 2018), and herald the beginning of a new branch of observational astronomy. With the two upcoming instruments KAGRA[3] (Somiya 2012) and LIGO-India[4] (Iyer et al. 2011; Unnikrishnan 2013; Abbott et al. 2016e), the network of advanced GW detectors is expected to continue making detections of GWs and answering fundamental questions about their astrophysical sources (Abbott et al. 2016e; Abbott et al. 2018).

In Gondán et al. (2018a), we determined the expected accuracy with which the aLIGO–AdV–KAGRA detector network may determine the eccentricity and other physical parameters of 10 $M_\odot$–10 $M_\odot$ and 30 $M_\odot$–30 $M_\odot$ precessing eccentric black hole—black hole (BH–BH) binaries. We found that measurement errors for the orbital eccentricity at formation, e_0, and eccentricity at the last stable orbit (LSO), e_{LSO}, can be as low as about $10^{-3} \times D_L/(1\,\mathrm{Gpc})$ and $10^{-4} \times D_L/(1\,\mathrm{Gpc})$, respectively, where D_L is the luminosity distance. Such low-eccentricity errors may give the aLIGO–AdV–KAGRA detector network the capability to distinguish among quasi-circular and low-eccentricity binaries and among different astrophysical formation channels.

In this paper, we extend Gondán et al. (2018a) to determine the expected measurement errors of e_0, e_{LSO}, and other physical parameters for precessing eccentric neutron star - neutron star (NS–NS), neutron star - black hole (NS–BH), and BH–BH binaries. We also determine the measurement error of the residual eccentricity $e_{10\mathrm{Hz}}$ at which the peak GW frequency (f_{GW}; Wen 2003) of binaries first enters the 10 Hz frequency band of advanced GW detectors. Further, we extend our investigations to a wide mass range of eccentric BH–BH binaries, and examine the measurement errors of binary parameters as a function of $e_{10\mathrm{Hz}}$.

The majority of NS–NS and NS–BH binaries may originate from isolated binaries in galactic fields (see Chruslinska et al. 2018; Kruckow et al. 2018; Vigna-Gómez et al. 2018 and references therein), and these binaries are expected to be well circularized by the time their GW signals enter the advanced detectors' frequency band (Kowalska et al. 2011). However, the eccentricity of binaries in the advanced detectors' frequency band may be non-negligible for many other astrophysical channels. These include tidal capture and collision of two NSs in globular clusters (GCs) that have undergone core collapse (Lee et al. 2010), binary–single interactions in GCs (Samsing et al. 2014), Kozai resonance in GCs (Thompson 2011) and galactic nuclei (GNs; Antonini & Perets 2012; Petrovich & Antonini 2017; Fragione et al. 2018), non-hierarchical triple systems in GCs and nuclear star clusters (Arca-Sedda et al. 2018), and close fly-bys between NSs and/or BHs in GNs can lead to the formation of eccentric NS–NS and NS–BH binaries due to GW emission (Kocsis et al. 2006; O'Leary et al. 2009; Kocsis & Levin 2012; Tsang 2013). These channels typically produce binaries with orbital eccentricities beyond $e_0 \gtrsim 0.9$ at formation, and depending on the pericenter distance at formation, these binaries may remain eccentric by the time

---

they enter the advanced GW detectors' frequency band (see e.g., Gondán et al. 2018b for details).

Previous parameter estimation studies of NS–NS and NS–BH binaries mostly focused on quasi-circular binaries (Cutler & Flanagan 1994; Poisson & Will 1995; Nicholson & Vecchio 1998; Nissanke et al. 2010; Cho et al. 2013; Chatziioannou et al. 2014; Favata 2014; O'Shaughnessy et al. 2014; Rodriguez et al. 2014; Berry et al. 2015; Canizares et al. 2015; Miller et al. 2015; Veitch et al. 2015; Farr et al. 2016; Vinciguerra et al. 2017; Coughlin et al. 2018; Dudi et al. 2018; Fan et al. 2018; Zhao & Wen 2018; Biwer et al. 2019) because their predicted merger rate densities are high. The recent detection of the first 10 GW transients constrain the merger rate density of NS binaries in the universe to 110–3840 Gpc^{-3} yr^{-1} (The LIGO Scientific Collaboration & the Virgo Collaboration 2018), which is consistent with previous rate predictions (Kalogera et al. 2004). With the non-detection of NS–BH binaries during the first and second observing runs, an upper limit of 610 Gpc^{-3} yr^{-1} is drawn for the merger rate density of such systems (The LIGO Scientific Collaboration & the Virgo Collaboration 2018), while recent estimates predict the merger rate density to be in the range 1–1500 Gpc^{-3} yr^{-1} (see Coward et al. 2012; Petrillo et al. 2013; Bauswein et al. 2014; Berger 2014; Siellez et al. 2014; de Mink & Belczynski 2015; Dominik et al. 2015; Fong et al. 2015; Jin et al. 2015; Kim et al. 2015; Belczynski et al. 2016a; Vangioni et al. 2016; Chruslinska et al. 2018 for recent rate predictions and Abadie et al. 2010 for a review of past estimates).

However, several theoretical studies have shown that the detection rates of eccentric NS–NS and NS–BH binaries may be non-negligible. Lee et al. (2010) showed that the merger rate density of tidal capture and collision of two NSs in GCs that have undergone core collapse (Fabian et al. 1975; Pooley et al. 2003; Grindlay et al. 2006) peak around $z \simeq 0.7$ at values of ~ 55 Gpc^{-3} yr^{-1} that drops to ~ 30 Gpc^{-3} yr^{-1} by $z = 0$. However, the rates are reduced for less optimistic NS retention fractions (Tsang 2013). Eccentric NS–NS and NS–BH binaries could result from hierarchical triples through the Kozai mechanism. This has been suggested to occur in mergers around supermassive BHs in GNs for NS–BH binaries with a merger rate density of 0.4 Gpc^{-3} yr^{-1} (Antonini & Perets 2012; Petrovich & Antonini 2017). Recently, Fragione et al. (2018) revisited these results and found an NS–BH and NS–NS merger rate density of 0.06–0.1 Gpc^{-3} yr^{-1} and 0.04–0.16 Gpc^{-3} yr^{-1}, respectively. Merger rate densities of ~ 0.7 Gpc^{-3} yr^{-1} can be expected from binary–single interactions from GCs (Samsing et al. 2014). Close fly-bys between NSs and/or BHs in GNs may result in eccentric NS–NS and NS–BH binaries with estimated merger rate densities of 0.04–6 Gpc^{-3} yr^{-1} and 0.05–0.6 Gpc^{-3} yr^{-1}, respectively (Tsang 2013).

While eccentric NS–NS and NS–BH binaries are expected to be rare compared to quasi-circular binaries, they are interesting for at least three reasons. First, significantly larger amounts of mass are ejected during eccentric NS–NS binary mergers than in quasi-circular NS–NS mergers (East & Pretorius 2012; Rosswog et al. 2013; Radice et al. 2016; Papenfort et al. 2018; Vivekanandji Chaurasia et al. 2018). Thus, despite being rare, they may nevertheless contribute a significant fraction of the overall r-process element abundances, and may give birth to bright electromagnetic emission in the infrared and radio bands relative to quasi-circular binaries. Additionally, eccentric NS–NS binaries produced by dynamical captures in dense stellar environments can potentially produce r-process nuclei at very

low metallicity and account for the r-process enhancements seen in some carbon-enhanced metal-poor stars (Ramirez-Ruiz et al. 2015).

A second reason eccentric NS–NS and NS–BH binaries are of interest is that they may improve the test of general relativity in the strong-field dynamics limit (Abbott et al. 2016a, 2016b, 2016c, 2016f, 2017a, 2017c). For eccentric binaries, a larger fraction of the energy is emitted in GWs at relativistic-velocities during pericenter passages than in quasi-circular inspirals (Loutrel et al. 2014). Thus, the GWs from eccentric binaries could capture effects from the highly nonlinear dynamical regime during pericenter passages.

Third, detections of many eccentric and quasi-circular NS–NS, NS–BH, and BH–BH binaries have the potential to constrain the astrophysical origin of GW source populations. The different formation channels leading to NS–NS, NS–BH, and BH–BH mergers may be distinguished using the measurement of the correlations between the orbital eccentricity and the chirp mass (Breivik et al. 2016), the correlation between the remnant mass and spins (Arca-Sedda & Benacquista 2019), the eccentricity in the LIGO/Virgo (Cholis et al. 2016; Samsing & Ramirez-Ruiz 2017; Arca-Sedda et al. 2018; Gondán et al. 2018b; Randall & Xianyu 2018a, 2018b; Samsing 2018; Zevin et al. 2018) and Laser Interferometer Space Antenna[5] (LISA) bands (Nishizawa et al. 2016, 2017; D'Orazio & Samsing 2018; Samsing & D'Orazio 2018) the spin orientations (Rodriguez et al. 2016; Farr et al. 2017; Liu & Lai 2017, 2018; Stevenson et al. 2017; Talbot & Thrane 2017; Vitale et al. 2017; Farr et al. 2018; Gerosa et al. 2018; Lopez et al. 2018), the effective spin parameter (Antonini et al. 2018; Ng et al. 2018; Schrøder et al. 2018; Zaldarriaga et al. 2018), the mass distribution (Stevenson et al. 2015; O'Leary et al. 2016; Mandel et al. 2017; Zevin et al. 2017; Fishbach et al. 2017), the spin distribution (Fishbach et al. 2017), and other waveform features (Meiron et al. 2017; Inayoshi et al. 2017; Kremer et al. 2018; Samsing et al. 2018). Further, kilonova signatures could provide information on the orbital properties of dynamically captured NS–NS binaries (Papenfort et al. 2018). See Section 5.4 in Barack et al. (2018) for an overview of ways to distinguish between different BH–BH merger source populations, including mergers in GNs and GCs.

Current search algorithms based on matched filtering are highly optimized for the detection of quasi-circular compact binary sources (see Abbott et al. 2016b, 2016c, 2017a, 2017b, 2017c, 2017d for a review of search algorithms) and burst-like GW signals (Abbott et al. 2016d). Several algorithms have been developed to recover the physical parameters of quasi-circular and burst-like sources (Cannon et al. 2012; Privitera et al. 2014; Cornish & Littenberg 2015; Littenberg & Cornish 2015; Veitch et al. 2015; Klimenko et al. 2016; Singer & Price 2016; Millhouse et al. 2018). However, GW sources that do not fall into these two categories may be missed by these search algorithms (Brown & Zimmerman 2010; Huerta & Brown 2013; Huerta et al. 2014; Tiwari et al. 2016; Huerta et al. 2018). The maximum eccentricity for a quasi-circular source to be detected with current techniques based on circular templates is ~ 0.1 (Brown & Zimmerman 2010; East et al. 2013; Huerta & Brown 2013; Huerta et al. 2014, 2017, 2018; Lower et al. 2018). Recently, several search methods have been developed to detect the waveforms of eccentric compact

---

[5] https://www.elisascience.org/

binaries (Tai et al. 2014; Coughlin et al. 2015; Tiwari et al. 2016), and the development of algorithms recovering the parameters of compact binaries on eccentric orbits is underway.

The paper is organized as follows. In Section 2 we summarize the method and describe the numerical setup we use to obtain the measurement errors for the physical parameters of precessing eccentric NS–NS and NS–BH binaries. We present our results in Section 3. Finally, we discuss our conclusions in Section 4. Details on the derivation of parameter measurement errors are presented in Appendices A and B.

In this paper, we use geometric units $c = G = 1$. We work in the observer frame assuming a binary at cosmological redshift z, and neglect peculiar velocity and weak-lensing effects (Kocsis et al. 2006). In this frame, all of the formulae have redshifted mass parameters $m_z = (1 + z)m$.

2. Methodology

In this section, we summarize the method we used to obtain the parameter measurement accuracy of GWs generated by precessing eccentric NS–NS and NS–BH binaries. We refer the reader for more details to Gondán et al. (2018a).

2.1. Waveform Model in Time Domain

We use the waveform model of Moreno-Garrido et al. (1994, 1995), which describes the quadrupole waveform emitted by a non-spinning binary on a Keplerian orbit undergoing slow pericenter precession. We ignore the radiation of higher multipole orders, which are typically subdominant at least in cases where the initial pericenter distance is not close to a grazing or zoom–whirl configuration and the initial velocity is much lower than the speed of light (Davis et al. 1972; Berti et al. 2010; Healy et al. 2016). For the time evolution of the orbital parameters semimajor axis and eccentricity, we adopt Peters (1964), who assumed quadrupole radiation and adiabatic evolution of orbital parameters. We include pericenter precession in the leading-order post-Newtonian (1PN) limit, which leads to a time-dependent angle of the pericenter. The time-domain waveform under these approximations is given explicitly in Mikóczi et al. (2012) and Gondán et al. (2018a). For simplicity, we restrict our attention to the repeated burst and eccentric inspiral phase and neglect the contribution of the tidal interaction and disruption, merger, and ringdown phases to the signal.[6]

2.2. Phases of Binary Evolution

We follow O'Leary et al. (2009) to characterize the binary orbit with its orbital eccentricity e and its dimensionless pericenter distance $\rho_p = r_p/M_{tot}$, which shrink strictly monotonically in time (Peters 1964). Here, r_p is the orbital separation between the two objects at pericenter, and M_{tot} is the total mass of the binary. When the orbital eccentricity is high $e \gtrsim 0.7$, the time-domain waveform consists of repeated bursts, which are

---

[6] Fully general-relativistic hydrodynamical simulations of highly eccentric NS–NS and NS–BH mergers (Stephens et al. 2011; East & Pretorius 2012; East et al. 2012, 2015, 2016; Gold et al. 2012; Dietrich et al. 2015; Paschalidis et al. 2015; Radice et al. 2016; Vivekanandji Chaurasia et al. 2018) and hydrodynamical simulations with Newtonian gravity of dynamical-capture NS–NS and NS–BH mergers (Lee et al. 2010; Piran et al. 2013; Rosswog et al. 2013) revealed that the outcome of such mergers significantly depends on the impact parameter and the intrinsic parameters of the binary, i.e., the component masses, the initial orbital eccentricity, the initial spins, and the NS equation of state.

Table 1
Locations and Orientations of the Considered GW Detectors in the Coordinate System Defined in Appendix B in Gondán et al. (2018a)

Detector	East Long.	North Lat.	Orientation ψ
LIGO H	$-119°.4$	$46°.5$	$-36°$
LIGO L	$-90°.8$	$30°.6$	$-108°$
VIRGO	$10°.5$	$43°.6$	$20°$
KAGRA	$137°.3$	$36°.4$	$65°$

Note. LIGO H marks the advanced LIGO detector in Hanford, WA, and LIGO L marks the advanced LIGO detector in Livingston, LA.

---

emitted during pericenter passages (Kocsis & Levin 2012). As the orbital eccentricity decreases due to GW emission, the GW signal changes into an eccentric inspiral waveform.

For precessing eccentric BH–BH sources, we truncate the waveform when the binary reaches the LSO, which we calculate in the leading-order approximation in the test-mass geodesic zero-spin limit for which $\rho_{p,LSO} = (6 + 2e_{LSO})/(1 + e_{LSO})$ (Cutler et al. 1994). Thus, we consider the waveform model between $0 < e_{LSO} < e < e_0 < 1$ or equivalently between $0 < \rho_{p,LSO} < \rho_p < \rho_{p0}$. Here we note that $4 < \rho_{p,LSO} < 6$ for $e_{LSO} \in [0, 1]$.

For precessing eccentric NS–NS and NS–BH sources, we account for the repeated burst and eccentric inspiral phase ignoring tidal effects and matter exchange among the components (Blanchet 2014). This approximation breaks down abruptly in the late inspiral phase, but they are reasonable in the earlier parts of the GW signal because of the steep separation dependence of these effects. Simulations of dynamical-capture NS–NS mergers show that tidal deformation and matter exchange become significant when the NSs first come into contact (Gold et al. 2012; East et al. 2012, 2016; Radice et al. 2016), which happens when $\rho_p \lesssim 8.5$ for non-spinning binaries (East et al. 2012). Simulations of dynamical-capture NS–BH mergers with an NS mass of $1.35\,M_\odot$ and a mass ratio of $q = 1/4$ (where $0 < q \leqslant 1$) in East et al. (2015) showed that binaries with $\rho_p \lesssim 6.5$ merge on the initial encounter, while those with $\rho_p \gtrsim 7.5$ go back out on a quasi-elliptic orbit after flyby. These limits shift down for higher-mass BHs because tidal effects on the NSs scale with $q^{-1/3}$; see Equation (3) in Lee et al. (2010). For precessing eccentric NS–NS and NS–BH binaries, we terminate the signal at $\rho_p = 8.5$ and 7.5, respectively. Note that this is a conservative estimate for NS–BH binaries with mass ratios well below $1/4$.

In the following, we refer to $\rho_{p,LSO}$ as the dimensionless pericenter distance at which the signal is terminated in our calculations as specified above and denote the corresponding eccentricity by e_{LSO}.

2.3. GW Detectors Used in the Analysis

Similar to Gondán et al. (2018a), we use the aLIGO–AdV–KAGRA detector network and adopt the design sensitivities for the two aLIGO (Abbott et al. 2016e), the AdV (Abbott et al. 2016e), and KAGRA (Somiya 2012) detectors.[7] The locations and orientations of these detectors are summarized in Table 1, and we define the orientation angle ψ for each detector as the angle measured clockwise from north between the x-arm of the detector and the meridian that passes through the position of

---

[7] Note, further, that the lower and upper limits of the advanced detector band are typically 10 Hz and 10^4 Hz, respectively.

the detector (see Appendix B in Gondán et al. 2018a for the geometric conventions of detectors). We assume that the noise in each detector is stationary colored Gaussian with zero mean, and that it is uncorrelated between the different detectors.

2.4. Parameters of Precessing Eccentric Binaries

The adopted waveform model involves 12 free parameters,[8] which are t_c, Φ_c, γ_c, θ_N, ϕ_N, θ_L, ϕ_L, $\ln D_L$, $\ln \mathcal{M}_z$, $\ln M_{\mathrm{tot},z}$, e_0 and e_{LSO}. Here, t_c is the coalescence time, Φ_c is the orbital phase at t_c, γ_c is the angle of periapsis at t_c, θ_N and ϕ_N are polar angles describing the sky position angles of the source in a coordinate system fixed relative to the center of the Earth such that $\theta_N = 0$ is along the geographic north pole and ϕ_N is along the prime meridian, θ_L and ϕ_L are the angular momentum vector direction angles in spherical coordinates defined similar to θ_N and ϕ_N, D_L is the luminosity distance between the center of the Earth and the GW source, $\mathcal{M}_z$ is the redshifted chirp mass at cosmological redshift z, $M_{\mathrm{tot},z}$ is the redshifted total mass at cosmological redshift z, e_0 is the orbital eccentricity at formation, and e_{LSO} is the eccentricity at the LSO.

The first 10 parameters (t_c, Φ_c, γ_c, θ_N, ϕ_N, θ_L, ϕ_L, $\ln D_L$, $\ln \mathcal{M}_z$, and $\ln M_{\mathrm{tot},z}$) are measurable independently for precessing nearly circular binaries, where γ_c and $M_{\mathrm{tot},z}$ dependence of the waveform is due to the first post-Newtonian effect of pericenter precession. Further, we showed in Gondán et al. (2018a) that e_0 and e_{LSO} can also be extracted from the waveform model if it leaves an imprint at the beginning and the end of the waveform, respectively (i.e., if the binary forms and the inspiral terminates in the advanced GW detectors' frequency band).

For the polar angles (θ_N, ϕ_N), we calculate and present the minor and major axes (a_N, b_N) of the corresponding 2D sky location error ellipse introduced in Lang & Hughes (2006). We do the same for the polar angles (θ_L, ϕ_L) by constructing the corresponding minor and major axes of the binary orientation error ellipse (a_L, b_L). We measure the errors for the rest of the parameters, where $\Delta D_L / D_L = \Delta(\ln D_L)$, and similarly for $\mathcal{M}_z$ and $M_{\mathrm{tot},z}$.

Note that the marginalized measurement errors of other parameters describing the source can be determined by linear combinations of the covariance matrix elements of the adopted parameters. For instance, the measurement error of $\rho_{\mathrm{p}0}$ is determined as

$$(\Delta \rho_{\mathrm{p}0})^2 = \left(\frac{\partial \rho_{\mathrm{p}}(e_0, e_{\mathrm{LSO}})}{\partial e_0} \right)^2 (\Delta e_0)^2$$
$$+ \left(\frac{\partial \rho_{\mathrm{p}}(e_0, e_{\mathrm{LSO}})}{\partial e_{\mathrm{LSO}}} \right)^2 (\Delta e_{\mathrm{LSO}})^2$$
$$+ 2 \frac{\partial \rho_{\mathrm{p}}(e_0, e_{\mathrm{LSO}})}{\partial e_0} \frac{\partial \rho_{\mathrm{p}}(e_0, e_{\mathrm{LSO}})}{\partial e_{\mathrm{LSO}}} \langle \Delta e_0 \Delta e_{\mathrm{LSO}} \rangle \tag{1}$$

because ρ_{p} can be expressed as a function of e_0 and e_{LSO} using the adopted adiabatic evolution equations and the equation defining the e_{LSO} (Gondán et al. 2018a). Here and in Equations (2) and (16) below, $\langle \Delta \lambda_i \Delta \lambda_j \rangle$ denotes the cross-correlation coefficient

---

[8] The logarithms are introduced for convenience in order to measure the relative errors, e.g., $(\Delta D_L)/D_L = \Delta(\ln D_L)$.

between the inferred parameter values λ_i and λ_j relative to their fiducial values.

Similarly, we express e_{10Hz} as a function of e_{LSO} and $M_{\mathrm{tot},z}$; see Appendix A for details. Its measurement error for binaries forming outside of the detector frequency bands is formally

$$(\Delta e_{\mathrm{10Hz}})^2 = \left(\frac{\partial e_{\mathrm{10Hz}}(e_{\mathrm{LSO}}, \ln M_{\mathrm{tot},z})}{\partial e_{\mathrm{LSO}}} \right)^2 (\Delta e_{\mathrm{LSO}})^2$$
$$+ \left(\frac{\partial e_{\mathrm{10Hz}}(e_{\mathrm{LSO}}, \ln M_{\mathrm{tot},z})}{\partial \ln M_{\mathrm{tot},z}} \right)^2 (\Delta \ln M_{\mathrm{tot},z})^2$$
$$+ 2 \frac{\partial e_{\mathrm{10Hz}}(e_{\mathrm{LSO}}, \ln M_{\mathrm{tot},z})}{\partial e_{\mathrm{LSO}}}$$
$$\times \frac{\partial e_{\mathrm{10Hz}}(e_{\mathrm{LSO}}, \ln M_{\mathrm{tot},z})}{\partial \ln M_{\mathrm{tot},z}} \langle \Delta e_{\mathrm{LSO}} \Delta \ln M_{\mathrm{tot},z} \rangle. \tag{2}$$

The NSs' equation of state leaves its imprint on the GW signal during the late stages of the inspiral when the two bodies are tidally distorted (Blanchet 2014), and during the merger and post-merger phases (Faber & Rasio 2012; Baiotti & Rezzolla 2017; Paschalidis & Stergioulas 2017). Thus, the tidal deformability information can be efficiently extracted from the late inspiral, merger, and post-merger phases of the waveform (Harry & Hinderer 2018). However, as already mentioned, for this first study of precessing eccentric NS–NS and NS–BH sources, we ignore the tidal deformabilities in this study for simplicity (Section 2.2).

Following Kocsis et al. (2007), we group the parameters as

$$\boldsymbol{\lambda}_{\mathrm{fast}} = \{ \Phi_c, t_c, \ln \mathcal{M}_z, \ln M_{\mathrm{tot},z}, \gamma_c, e_{\mathrm{LSO}} \}, \tag{3}$$

$$\boldsymbol{\lambda}_{\mathrm{slow}} = \{ \ln D_L, \theta_N, \phi_N, \theta_L, \phi_L \}, \tag{4}$$

where the $\boldsymbol{\lambda}_{\mathrm{fast}}$ fast parameters are related to the high-frequency GW phase, while the $\boldsymbol{\lambda}_{\mathrm{slow}}$ slow parameters appear only in the slowly varying amplitude of the GW signal. Slow parameters are mostly determined from a comparison of the GW signals measured by the different detectors in the network.

2.5. Mass Ranges

We set the lower bound of the BH mass range of interest to 5 $M_\odot$ according to the observations of X-ray binaries (Bailyn et al. 1998; Özel et al. 2010; Farr et al. 2011; Belczynski et al. 2012). In order to set the upper bound, we consider the following arguments: (i) supernova theory (Belczynski et al. 2014, 2016b; Marchant et al. 2016; Gilmer et al. 2017; Mapelli et al. 2017; Woosley 2017) predicts a mass gap between ~50 $M_\odot$ and ~135 $M_\odot$ in the BH initial mass function, (ii) studies based on the current GW observations of BH mergers and population synthesis find that the gap may start between ~40 $M_\odot$ and ~76 $M_\odot$ (Fishbach & Holz 2017; Bai et al. 2018; Giacobbo et al. 2018), and (iii) the evolution of the BH initial mass function may fill the mass gap due to mergers of BHs but drops off quickly beyond ~100 $M_\odot$ (Christian et al. 2018). Since the mass function of stellar-mass BHs is still uncertain and systems more massive than a few times 100 $M_\odot$ will not lie in the most sensitive band of aLIGO-type instruments during the eccentric inspiral, we do not consider systems beyond ~110 $M_\odot$ in this paper.

For NSs, statistical analyses based on observations of millisecond pulsars, double NS systems, and X-ray binaries predict a bimodal mass distribution with a sharp and dominant peak at $\sim 1.35\ M_\odot$ (Valentim et al. 2011; Özel et al. 2012; Kiziltan et al. 2013; Antoniadis et al. 2016; Özel & Freire 2016; Alsing et al. 2018). We set the NS mass to 1.35 $M_\odot$ in this study.

We note that we validated the codes in a larger mass range for component masses between 1 $M_\odot$ and $110\,M_\odot$ (Sections 2.6 and 2.9).[9]

2.6. Waveform Model in Frequency Domain

The expressions defining the signal-to-noise ratio (S/N) and the Fisher matrix components are both given in Fourier space, hence we calculate the Fourier transform of the adopted time-domain measured signal. The time-dependent GW signal measured by the kth detector can be given as

$$h_k(t) = h_+(t)F_{+,k}[\theta_N(t), \phi_N, \theta_L, \phi_L] + h_\times(t)F_{\times,k}[\theta_N(t), \phi_N, \theta_L, \phi_L], \qquad (5)$$

where $h_+(t)$ and $h_\times(t)$ are the two polarization states of the adopted waveform model defined in Section 2.1, and $F_{+,k}$ and $F_{\times,k}$ are the antenna factors of the kth detector quantified in Appendix B in Gondán et al. (2018a). Because we ignore spins in this study, the angular momentum vector direction (θ_L, ϕ_L) is conserved during the eccentric inspiral (Cutler & Flanagan 1994).

The polar angle of the source θ_N relative to the detector depends on the rotation phase of the Earth during the day, hence, Earth's rotation may in principle leave an imprint on the signal. To see if this may be significant, we determine the total time the GW signal spends in the advanced GW detectors' frequency band for different harmonics as a function of ρ_{p0} following Gondán et al. (2018a). In comparison with the analysis presented in Appendix C in Gondán et al. (2018a), we extend the component mass range to $[1\,M_\odot, 110\,M_\odot]$ (Section 2.5), and we draw e_0 between [0.9, 1[in order to investigate binaries that enter the advanced GW detectors' frequency band with moderate or high eccentricities. We find that for high ρ_{p0}, the signal effectively circularizes by the time it enters the advanced GW detectors' frequency band, and it spends seconds to several minutes in the advanced detectors' frequency band (see also Kocsis & Levin 2012). For lower ρ_{p0} (i.e., when binaries enter the advanced GW detectors' frequency band with moderate or high eccentricities), the signal may spend up to several hours in the detector bands.[10] However, more than $\sim 99\%$ of the S/N accumulates in only a few seconds to a few$\times 10$ of minutes; see Appendix C in Gondán et al. (2018a) for details. Thus, the Earth's rotation and orbit around the Sun may help to decrease the parameter

measurement errors only for rare very high SNR events, but in most cases, this can be neglected for precessing eccentric NS–NS, NS–BH, and BH–BH binaries. In this paper, we neglect these low SNR modulation effects.

2.7. Parameter Values for Calculations as a Function of ρ_{p0}

Here we list the assumed parameter values for calculations used to measure the S/N and parameter measurement errors as a function of ρ_{p0} and $e_{10\,\mathrm{Hz}}$, respectively.

First, we carry out simulations for precessing eccentric NS–NS, NS–BH, and BH–BH binaries in which we examine the e_0, ρ_{p0}, and component mass dependent properties of the total network S/N (S/N$_{\mathrm{tot}}$, see Section 4 in Gondán et al. 2018a) and the measurement errors of binary parameters. To do so, we determine these quantities as a function of ρ_{p0} for arbitrarily fixed component masses, luminosity distance, binary direction and orientation angles, and orbital eccentricity at formation as follows.

We present the results of our analysis for an arbitrary choice of angular parameters $\theta_N = \pi/2$, $\phi_N = \pi/3$, $\theta_L = \pi/4$, and $\phi_L = \pi/5$. Further, to explore the range of parameter errors, we repeated our calculations for 100 other randomly chosen angles by drawing $(\cos\theta_N, \cos\theta_L)$ and (ϕ_N, ϕ_L) from isotropic distributions between $[-1, 1]$ and $[0, 2\pi]$, respectively. We preformed the calculations for $D_L = 100$ Mpc, and scaled the results for an arbitrary choice of D_L up to 1 Gpc.[11] We present results for $e_0 = 0.9$ at any given ρ_{p0} and also examine higher e_0 values $(0.9 < e_0 < 1)$ to show that the results are not very sensitive to this assumption (Gondán et al. 2018a). By increasing ρ_{p0} beyond the value where the binary forms in the band, we cover the full possible range of eccentricities at the point when the binary enters the detector frequency bands (Section 2.8). We assume the fiducial value $t_c = \Phi_c = \gamma_c = 0$ because these parameters are responsible for an overall phase shift of the waveform and thus did not randomize their values (Gondán et al. 2018a).

After fixing the component masses, m_A and m_B, and the luminosity distance, D_L, the redshifted mass parameters $\mathcal{M}_z$ and $M_{\mathrm{tot},z}$ can be given as $\mathcal{M}_z = (1 + z)(m_A m_B)^{3/5}(m_A + m_B)^{-1/5}$ and $M_{\mathrm{tot},z} = (m_A + m_B)(1 + z)$, respectively. By assuming a flat ΛCDM cosmology, z is calculated numerically as

$$D_L = \frac{(1+z)c}{H_0}\int_0^z \frac{dz'}{\sqrt{\Omega_{\mathrm{M}}(1 + z')^3 + \Omega_\Lambda}}, \qquad (6)$$

where $H_0 = 68\ \mathrm{km\ s^{-1}Mpc^{-1}}$ is the Hubble constant, and $\Omega_{\mathrm{M}} = 0.304$ and $\Omega_\Lambda = 0.696$ are the density parameters for matter and dark energy, respectively (Planck Collaboration et al. 2014a, 2014b).

Following Gondán et al. (2018a), we set the lower bound of the ρ_{p0} range of interest to 5 for BH–BH binaries. Further, for NS–NS and NS–BH binaries, the lower bound of the ρ_{p0} range is set to 9 and 8, respectively, according to the ρ_p cutoffs; see Section 2.2 for details. These low values are likely for eccentric BH–BH binaries (see Gondán et al. 2018a for a summary of channels), and also likely for eccentric NS–NS and NS–BH sources that form through the GW capture mechanism in high-velocity dispersion environments such as GNs and GCs

---

[9] Here, the lower bound corresponds to the estimated minimum mass of NSs (Valentim et al. 2011; Özel et al. 2012; Kiziltan et al. 2013; Antoniadis et al. 2016; Özel & Freire 2016; Alsing et al. 2018), the upper bound corresponds to the above considered upper bound of the BH mass range of interest, and we ignore the mass gap between NSs and BHs, i.e., between 2.17 $M_\odot$ (see Margalit & Metzger 2017 and references therein) and 5 $M_\odot$.

[10] For instance, higher orbital harmonics of the signal for an eccentric NS–NS binary with $e \sim 0.9$ and $\rho_{p0} = 150$, which forms inside the advanced GW detectors' frequency band (Section 2.8), spend up to 2×10^4 s in the bands; see Appendix C in Gondán et al. (2018a) for details of these calculations. The maximum time in a band scales with M_{tot} (Kocsis & Levin 2012; Gondán et al. 2018a).

[11] The parameter measurement errors and the S/N$_{\mathrm{tot}}$ roughly scale as $\propto D_L$ and $\propto 1/D_L$, respectively, between 100 Mpc and 1 Gpc; see Appendix B for details.

(O'Leary et al. 2009), tidal capture during close encounters in GCs that underwent core collapse (Lee et al. 2010), binary–single interaction in GCs (Samsing et al. 2014), and dynamical multi-body interaction in the core-collapsed regions of star clusters without a central massive BH (Antonini & Rasio 2016). We refer to the circular limit by setting $e_0 \to 0$ for arbitrary fixed ρ_{p0} or $\rho_{p0} \to \infty$ for arbitrary fixed $e_0 \leqslant 1$; see Figure 5 in O'Leary et al. (2009). In practice, we set $\rho_{p0} = 800$. We set the upper bound of the ρ_{p0} range to this value because in this case, binaries are expected to be well circularized by the time their peak GW frequency enters the advanced GW detectors' frequency band over the considered ranges of component mass and e_0.

2.8. Calculations as a Function of $e_{10\,\mathrm{Hz}}$

The orbital parameters ρ_p and e both shrink due to GW emission (Peters 1964), while f_{GW} continuously increases with shrinking ρ_p and e (Wen 2003). As a consequence, binaries in the above introduced analysis that have high ρ_{p0} enter the advanced GW detectors' frequency band with relatively low residual eccentricities, while those with relatively low ρ_{p0} form in the advanced GW detectors' frequency band. Recent studies (Brown & Zimmerman 2010; East et al. 2013; Huerta & Brown 2013; Huerta et al. 2014, 2017, 2018; Lower et al. 2018) have shown that the classification of binaries as quasi-circular or eccentric binaries depends on this eccentricity, i.e., an eccentric binary can be misclassified as quasi-circular binary if the residual eccentricity exceeds ~ 0.1. Therefore, similar to the analysis presented in Section 2.7, we carry out simulations for precessing eccentric NS–NS, NS–BH, and BH–BH binaries in which we examine the $e_{10\,\mathrm{Hz}}$ and component mass dependent properties of the S/N_{tot} and the measurement errors of binary parameters.

For binaries that form outside of the advanced GW detectors' frequency band, it is customary to define the measurement errors of binary parameters as a function of $e_{10\,\mathrm{Hz}}$ when the peak GW frequency first enters the advanced GW detectors' frequency band, i.e., $f_{GW} = f_{det} = 10$ Hz. Here, we adopt Wen (2003) to define f_{GW} as

$$f_{GW} = \frac{2(1+e)^{1.1954}}{(1-e^2)^{3/2}} \frac{M_{tot,z}^{1/2}}{2\pi a^{3/2}}. \quad (7)$$

For each component mass and e_0 defined in Section 2.7, we determine the initial dimensionless pericenter distance $\rho_{p0,det}$ below which binaries form within the advanced GW detectors' frequency band. Using $a(1-e) = M_{tot,z}\rho_p$ and Equation (7), we find that

$$\rho_{p0,det} = ((1+e_0)^{0.3046}\pi M_{tot,z}f_{det})^{-2/3}, \quad (8)$$

which reduces in the $e_0 \to 1$ limit to (Gondán et al. 2018b)

$$\rho_{p0,det} = 40.9 \left(\frac{M_{tot,z}}{20\,M_\odot}\right)^{-2/3} \left(\frac{f_{det}}{10\,\mathrm{Hz}}\right)^{-2/3}. \quad (9)$$

Next, we calculate ρ_{p0} as a function of $e_{10\,\mathrm{Hz}}$ at fixed component masses and e_0 in order to carry out simulations similar to those presented in Section 2.7, but by initializing them with $e_{10\,\mathrm{Hz}}$ through ρ_{p0}. We evolve systems from their initial orbital parameters using the evolution equations of Peters (1964), therefore the function $\rho_p \equiv \rho_p(e_0, \rho_{p0}, e)$ is known for any initial

condition; see Equation (20). After combining Equation (7) and $a(1-e) = M_{tot,z}\rho_p$ together with $\rho_p(e_0, \rho_{p0}, e)$, ρ_{p0} can be given for binaries forming outside of the detector frequency bands (i.e., $\rho_{p0} \geqslant \rho_{p0,det}$) as a function of $e_{10\,\mathrm{Hz}}$ at fixed e_0 and $M_{tot,z}$ by solving numerically the equation $f_{det} = f_{GW}$ for ρ_{p0}, which can be written as

$$f_{det} = [(1+e_{10\,\mathrm{Hz}})^{0.3046}M_{tot,z}\pi[\rho_p(e_{10\,\mathrm{Hz}}, e_0, \rho_{p0})]^{3/2}]^{-1}. \quad (10)$$

For these calculations involving $e_{10\,\mathrm{Hz}}$, we focus on the range of $e_{10\,\mathrm{Hz}}$ between $[8 \times 10^{-4}, 0.9]$. For each choice of component masses and initial orbital eccentricity, we calculate the corresponding ρ_{p0} using Equation (10), and use these values to evaluate the S/N_{tot} and the measurement errors of binary parameters. Other parameters are chosen as in Section 2.7.

2.9. Validation of Codes for NS–NS, NS–BH, and BH–BH Binaries

We adopt the same computationally efficient formulae to calculate the S/N and the Fisher matrix components that were derived and validated in Appendices D and E in Gondán et al. (2018a). It was shown that the results of these codes for the S/N_{tot} and the measurement errors of binary parameters are qualitatively consistent with those presented in previous studies (Arun et al. 2005; O'Leary et al. 2009; Yunes et al. 2009; Kyutoku & Seto 2014; Sun et al. 2015; Ma et al. 2017); see Section 6.3 in Gondán et al. (2018a) for details. We repeated the validation tests of the source codes for precessing eccentric NS–NS and NS–BH sources with the corresponding ρ_p cutoffs (Section 2.1) by drawing the component masses between $1\,M_\odot$ and $110\,M_\odot$ (Section 2.5) with all other parameter ranges and distributions fixed as in Appendix E in Gondán et al. (2018a). We found similar trends with those presented in Gondán et al. (2018a). This justifies using the same codes to calculate the S/N and the Fisher matrix components for precessing NS–NS and NS–BH binaries on eccentric inspiraling orbits given the approximations listed above.

3. Results

We start with a brief summary of results on the parameter errors as a function of system parameters in Section 3.1 and present details in the following subsections. In Section 3.2 we present the measurement errors of eccentricity at different stages of the binary evolution and the initial dimensionless pericenter distance. In Section 3.3 we show the measurement errors for source distance, sky location, binary orientation, and redshifted chirp mass. Next, in Section 3.4 we present results for the measurement accuracy of the characteristic relative velocity of the sources. In Sections 3.5 and 3.6 we discuss the initial orbital parameter and mass dependence of measurement errors, respectively. Finally, in Section 3.7 we present measurement errors of various source parameters for fixed S/N_{tot}.

3.1. Overview of Results

Figure 1 shows our findings for the S/N_{tot} and Figures 2–9 show the measurement errors of binary parameters for precessing eccentric NS–NS, NS–BH, and BH–BH binaries using the aLIGO–AdV–KAGRA GW detector network. These figures display the dependences of measurement errors on ρ_{p0}, $e_{10\,\mathrm{Hz}}$,
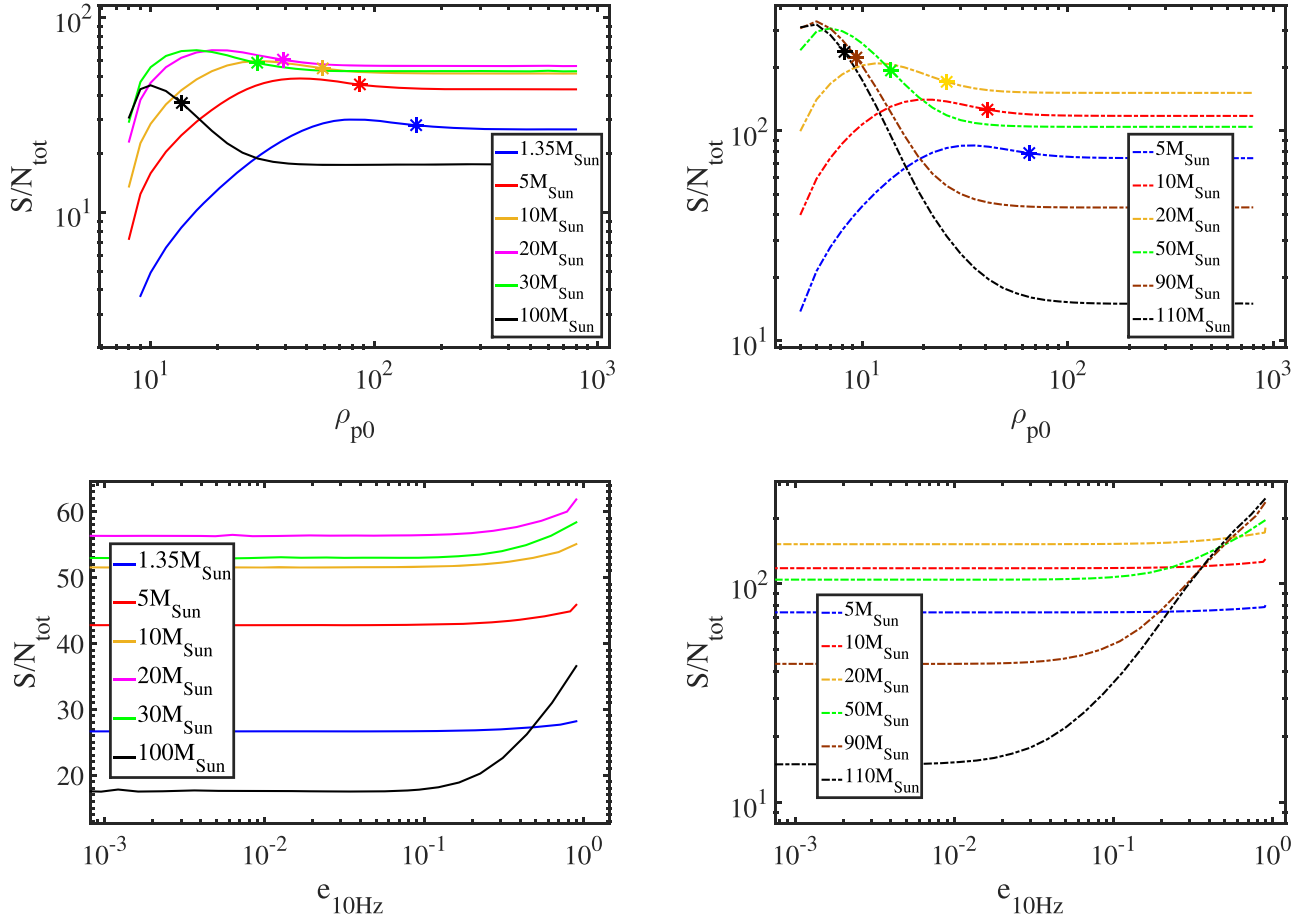
Figure 1. Total GW network S/N (S/N_{tot}) for precessing eccentric NS–NS and NS–BH binaries (left panels) and precessing, eccentric, equal-mass BH–BH binaries (right panels) as a function of their initial dimensionless pericenter distance ρ_{p0} for initial eccentricity $e_0 = 0.9$ (top panels) and as a function of their eccentricity $e_{10\,Hz}$ at which the peak GW frequency (f_{GW}; Wen 2003) $f_{GW} = 10$ Hz (bottom panels). In the left panels, the NS mass is 1.35 $M_\odot$ and the mass of the companion is labeled in the legend. For each curve in the top panels, a star indicates $\rho_{p0,det}$ defined as the ρ_{p0} at which f_{GW} first enters the advanced GW detectors' frequency band at 10 Hz; see Section 2.8 for details. Binaries with $\rho_{p0} \leqslant \rho_{p0,det}$ have $f_{GW} \geqslant 10$ Hz and form inside the advanced GW detectors' frequency band. The bottom panels show binaries where the binaries form outside of the advanced GW detectors' frequency band with $\rho_{p0} \geqslant \rho_{p0,det}$. The source direction and orientation angular parameters are fixed arbitrarily at $\theta_N = \pi/2$, $\phi_N = \pi/3$, $\theta_L = \pi/4$, and $\phi_L = \pi/5$ (see Table 1 for the parameters of the detector network). Results are displayed for $D_L = 100$ Mpc, which may be calculated for other source distances as $S/N_{tot} \times (100\ \text{Mpc}/D_L)$. The accuracy of this scaling is 5%–12% (7%–17%) for 500 Mpc (1 Gpc); see Appendix B for details. We find similar trends with ρ_{p0} for other random choices of binary direction and orientation (not shown). The maximum of S/N_{tot} is sensitive to the binary mass and converges asymptotically to the circular limit for high ρ_{p0} and for low $e_{10\,Hz}$.

and binary component masses. Figure 1 shows the S/N_{tot} as a function of ρ_{p0} and $e_{10\,Hz}$ for all types of binaries of different masses. Figure 2 shows the ρ_{p0} dependence of the parameter measurement errors for ($\Delta \ln \mathcal{M}_z$, $\Delta \ln D_L$, a_N, b_N, a_L, b_L) for precessing eccentric NS–NS and NS–BH binaries of different BH masses, while Figure 3 shows that for parameters (Δe_0, $\Delta \rho_{p0}$, Δe_{LSO}). In these figures the asymptotic limit of high ρ_{p0} represents the case of circular binaries. Decreasing ρ_{p0} from infinity corresponds to binaries that form outside the GW detectors' frequency band at $f_{GW} = 10$ Hz with $e_0 = 0.9$ and enter the frequency bands with some lower eccentricity $e_{10\,Hz} < e_0$ (the value of $e_{10\,Hz}$ is not shown in this figure, it is higher for lower ρ_{p0}), while even smaller ρ_{p0} below the star symbols in the figure represents cases where the GW-driven evolution with $e_0 = 0.9$ starts within the detector band. Similarly, Figures 4 and 5 show the ρ_{p0} dependence of parameter measurement errors for precessing eccentric BH–BH binaries of different masses. Figures 6–9 are analogous to Figures 2–5, but show the parameter measurement errors as a function of $e_{10\,Hz}$ instead of ρ_{p0} and include an additional

panel for $\Delta e_{10\,Hz}$. In particular, Figures 6 and 7 show parameter measurement errors as a function of $e_{10\,Hz}$ for precessing eccentric NS–NS and NS–BH binaries, and Figures 8 and 9 show those for precessing eccentric BH–BH binaries. Figure 10 displays results for the measurement accuracy of the characteristic relative velocity w of the sources before GWs start driving the evolution v^{12} (see Equation 12 below) as a function of ρ_{p0} and $e_{10\,Hz}$ for precessing eccentric NS–NS, NS–BH, and BH–BH binaries. Results for the S/N_{tot} and the measurement errors of binary parameters $\Delta\lambda$ are displayed for $D_L = 100$ Mpc, but can be scaled to other D_L values as $S/N_{tot} \times (100\ \text{Mpc}/D_L)$ and $\Delta\lambda \times (D_L/100\ \text{Mpc})$ with an inaccuracy level of 7%–17% and 5%–21% at 1 Gpc, respectively; see Appendix B for details. Note that the positions of the stars correspond to $D_L = 100$ Mpc, and they shift in the figure for higher redshift as $(1 + z)^{-2/3}$ (see Equation 8).

---

[12] This is expected to be comparable to the characteristic velocity dispersion of the host environment.
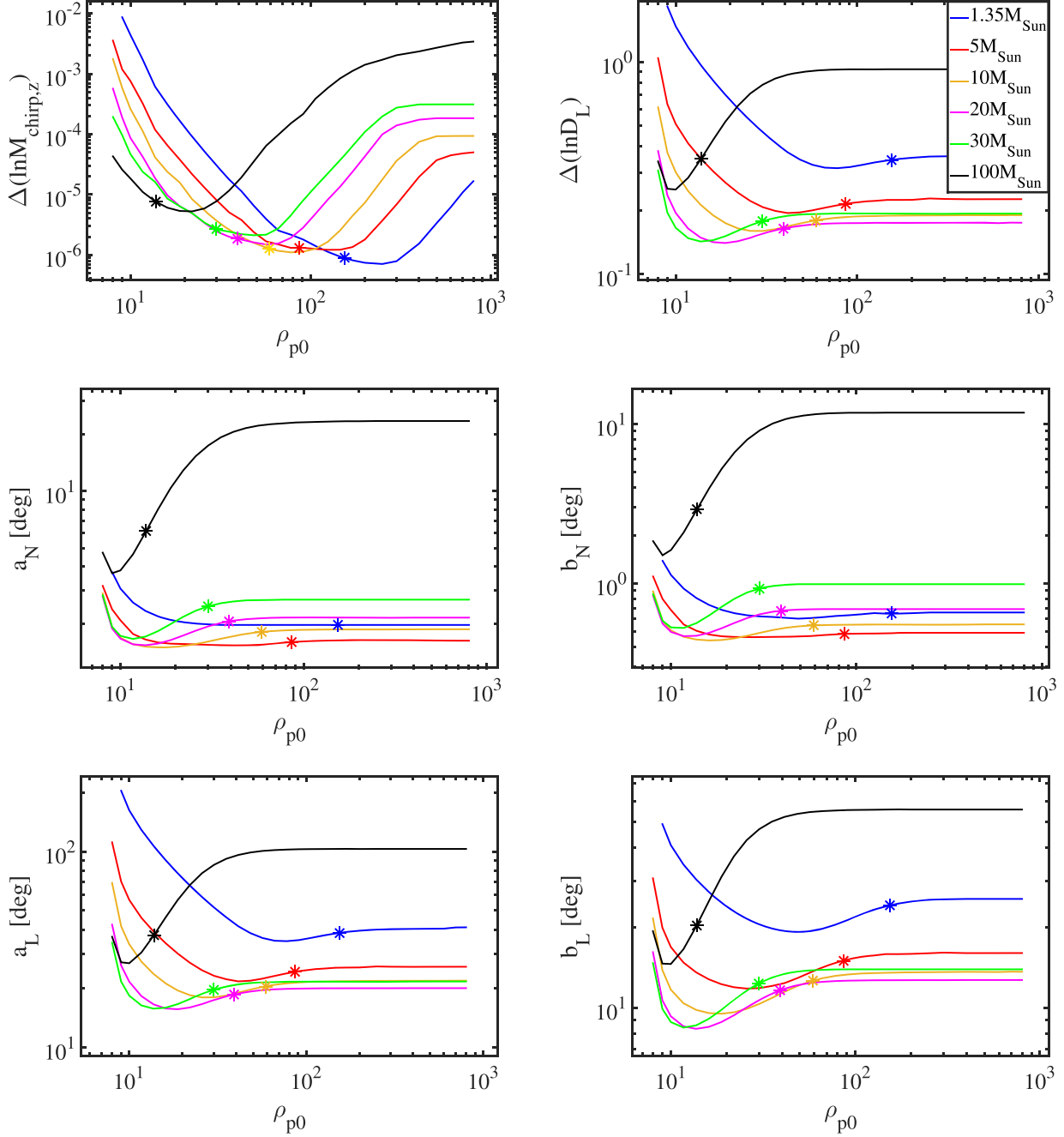
Figure 2. Measurement errors of various source parameters as a function of ρ_{p0} for precessing eccentric NS–NS and NS–BH binaries with different companion masses as shown in the legend with all other binary parameters fixed as in the left panel of Figure 1. Stars indicate the case where the binary forms at $f_{GW} = 10$ Hz as in Figure 1. The binary parameter measurement errors are displayed for $D_L = 100$ Mpc, but can be scaled to other D_L values by multiplying the displayed results by a factor of $D_L/100$ Mpc. This scaling is accurate to within 3%–15% (5%–21%) for 500 Mpc (1 Gpc); see Appendix B for details. First row left: Redshifted chirp mass, $\Delta\mathcal{M}_z/\mathcal{M}_z = \Delta(\ln\mathcal{M}_z)$. First row right: Luminosity distance $\Delta D_L/D_L = \Delta(\ln D_L)$. Second row: Semimajor (left) and semiminor (right) axes of the sky position error ellipse, a_N and b_N. Third row: Semimajor (left) and semiminor (right) axes of the error ellipse for the binary orbital plane normal vector direction, a_L and b_L. The measurement errors converge asymptotically to the circular limit for high ρ_{p0}. We find similar trends with ρ_{p0} for other random choices of binary direction and orientation (not shown).

Figures 11 and 12 show the measurement errors for the parameters (e_0, ρ_{p0}, $e_{10\,Hz}$, e_{LSO}, $\ln\mathcal{M}_z$, $\ln D_L$, $\ln w$) for a reference S/N$_{tot}$ of 20 and display the measurement errors as a function of $e_{10\,Hz}$ for precessing eccentric NS and BH binaries. Note, further, that these results can be approximately scaled to other S/N$_{tot}$ values by multiplying the results by a factor of $20 \times$ S/N$_{tot}^{-1}$.

3.2. Measurement Errors of Eccentricity and Initial Dimensionless Pericenter Distance

Our conclusions on the eccentricity and initial dimensionless pericenter distance errors are as follows:

1. The measurement error of the eccentricity at $f_{GW} = 10$ Hz is at the level of $\Delta e_{10\,Hz} \sim (10^{-4} - 10^{-3}) \times (D_L/100\,Mpc)$ for precessing eccentric NS–NS, NS–BH, and
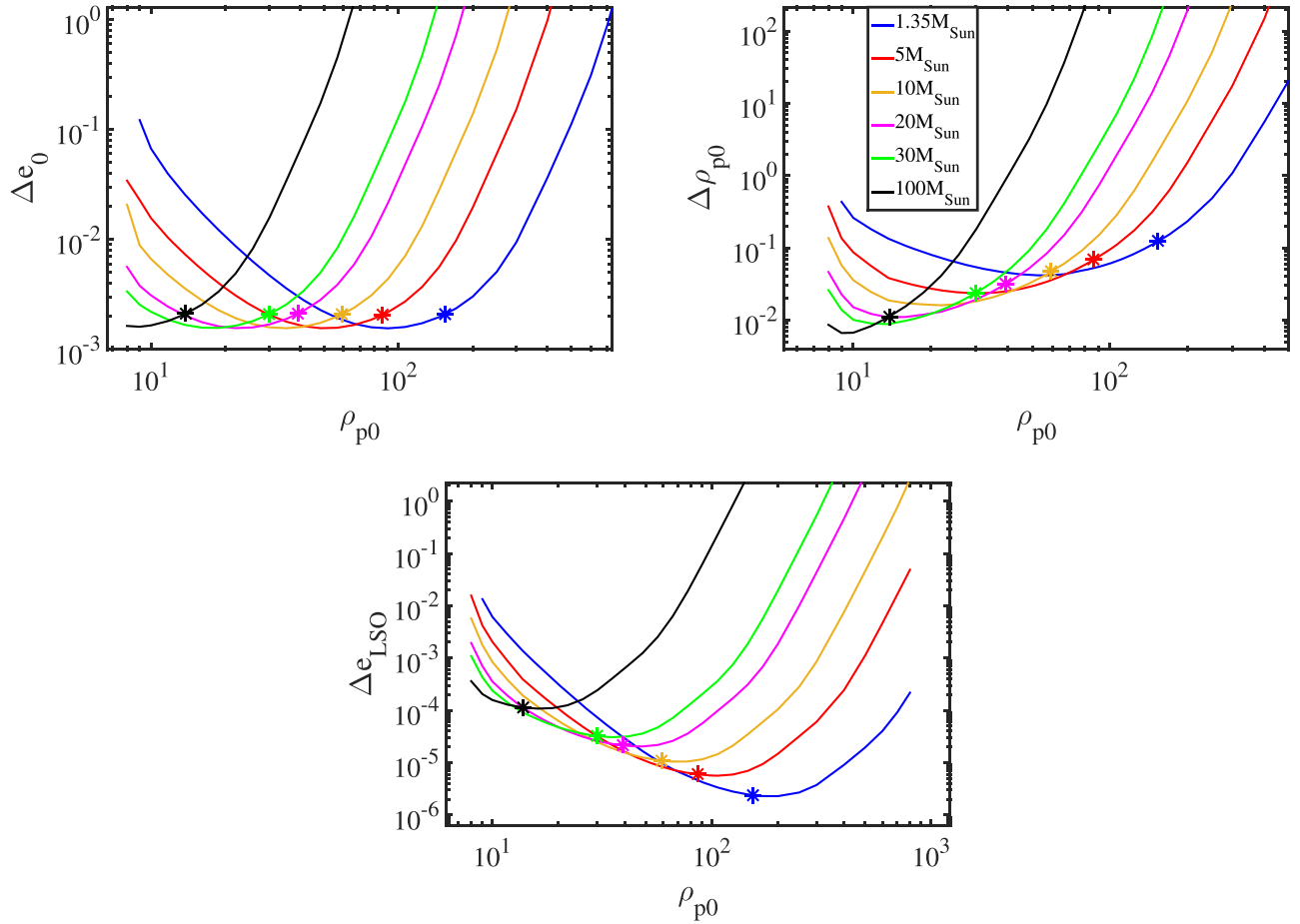
Figure 3. Same as Figure 2, but showing the NS–NS and NS–BH binary measurement errors for source parameters specific to eccentric binaries: initial eccentricity Δe_0 (top left panel), initial dimensionless pericenter distance $\Delta \rho_{p0}$ (top right panel), and eccentricity at the last stable orbit, Δe_{LSO} (bottom panel). The measurement error of these parameters increases rapidly for high ρ_{p0}. The measurement error of Δe_{LSO} is inaccurate for high ρ_{p0} because the Fisher matrix algorithm becomes invalid in this regime (Gondán et al. 2018a). Similar to Figure 2, results are displayed for $D_L = 100$ Mpc, but may be scaled to other D_L values by multiplying the displayed results by a factor of $D_L/100$ Mpc. We find similar trends with ρ_{p0} for other random choices of binary direction and orientation (not shown).

BH–BH binaries if $e_{10\,Hz} \gtrsim 0.1$ (Figures 7 and 9). These errors improve systematically for lower binary masses.[13]

2. The orbital eccentricity of a binary may be detected to be significantly different from zero if $e_{10\,Hz} \gtrsim \Delta e_{10\,Hz}$. We find that the minimum eccentricity where this is satisfied can be estimated roughly as

$$e_{10\,Hz,min} \simeq 0.04 \times \left(\frac{D_L}{100\,\text{Mpc}}\right)^{0.2}$$
$$\times \left(\frac{M_{tot,z}}{100\,M_\odot}\right)^{0.1} \times \left(\frac{\eta}{0.25}\right)^{0.03}, \quad (11)$$

where η is the symmetric mass ratio defined as $\eta = m_A m_B/(m_A + m_B)^2$.[14] This estimate is based on masses and distances of simulated binaries using the median of $\Delta e_{10\,Hz}$, obtained for the 100 randomly generated sky position and angular momentum unit

vectors (Section 2.8). For eccentric sources with masses and distances that match the currently reported 10 GW sources (GW150914, GW151226, GW170104, GW170608, GW170729, GW170809, GW170814, GW170817, GW170818, and GW170823; Abbott et al. 2016b, 2016c, 2017a, 2017b, 2017c, 2017d; The LIGO Scientific Collaboration & the Virgo Collaboration 2018), we find that $e_{10\,Hz}$ may be measured to be nonzero using the aLIGO–AdV–KAGRA detector network at design sensitivity if $e_{10\,Hz} \gtrsim \{0.051, 0.046, 0.058, 0.043, 0.081, 0.063, 0.053, 0.023, 0.062, 0.072\}$, respectively.

We may compare these results with recent studies, which employed an overlap method (Huerta et al. 2018; Lower et al. 2018) and model selection (Lower et al. 2018), to examine the capability to detect deviations from quasi-circularity. Our results for GW150914 match that of Lower et al. (2018) to within ~2% and our results for GW150914, GW151226, GW170104, GW170814, and GW170608 are a factor of ~3–4 lower than those presented by Huerta et al. (2018), who used different assumptions on the detector network, and a different analysis method and waveform model. In particular, Huerta et al. (2018) considered one aLIGO detector and spinning, quasi-circular templates in their analysis, while we considered the aLIGO-AdV-KAGRA detector network

---

[13] This is qualitatively consistent with the findings of Sun et al. (2015). Note, however, that only a qualitative comparison is possible because Sun et al. (2015) considered a different detector network, applied a different waveform model, and used different definitions for both e_0 and ρ_{p0}.

[14] This expression is valid at least up to 1 Gpc, which is the distance limit below which we validated our codes (Section 2.9) and determined numerically how the S/N$_{tot}$ and the parameter measurement errors scale with D_L (Appendix B).
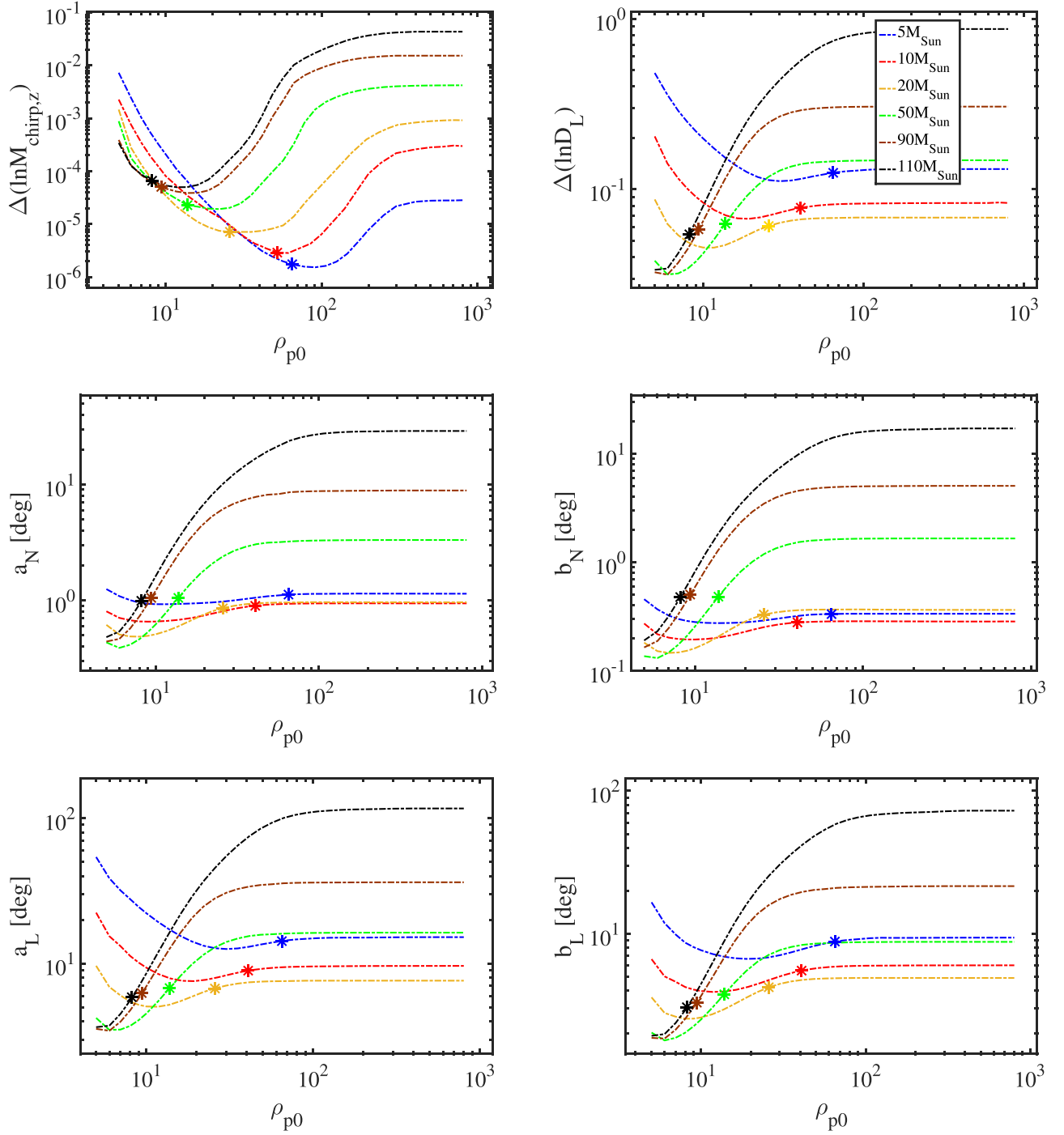
Figure 4. Same as Figure 2, but for precessing, eccentric, equal-mass BH–BH binaries of different masses with all binary parameters fixed as in the right panels of Figure 1. Binaries form in the detector's frequency band to the left of the stars.

and a non-spinning waveform model, which may be responsible for a substantial part of the discrepancy.

3. Figures 7 and 9 show that the eccentricity at the LSO can be measured to an exquisite precision with the aLIGO–AdV–KAGRA detector network at design sensitivity at the level of $\Delta e_{\rm LSO} \sim (10^{-5} - 10^{-4}) \times (D_{\rm L}/100\ {\rm Mpc})$ and $\Delta e_{\rm LSO} \sim 10^{-3} \times (D_{\rm L}/100\ {\rm Mpc})$ for precessing eccentric BH–BH binaries with component masses below and above $50\ M_\odot$, respectively, if $e_{10\ {\rm Hz}} \gtrsim 0.1$. The measurement errors for $e_{\rm LSO}$ are even better for precessing eccentric NS–NS binaries and NS–BH binaries with BH masses below $\sim 10\ M_\odot$ and

reach $\Delta e_{\rm LSO} \sim (10^{-6} - 10^{-5}) \times (D_{\rm L}/100\ {\rm Mpc})$. The eccentricity errors improve systematically for lower binary masses and higher $e_{10\ {\rm Hz}}$ values for all types of binaries. The magnitude of $\Delta e_{\rm LSO}$ is somewhat worse for binaries that form well inside the advanced GW detectors' frequency band than those that form at the lower edge of the band (i.e., $f_{\rm GW} \sim 10$ Hz), as shown in Figures 3 and 5 (i.e., left of stars therein).

4. $\Delta e_{\rm LSO}$ and $\Delta e_{10\ {\rm Hz}}$ have a weak $e_{10\ {\rm Hz}}$ dependence for all types of binaries if $e_{10{\rm Hz}} \gtrsim 0.2$ (Figures 7 and 9). The eccentricity measurement errors increase if decreasing
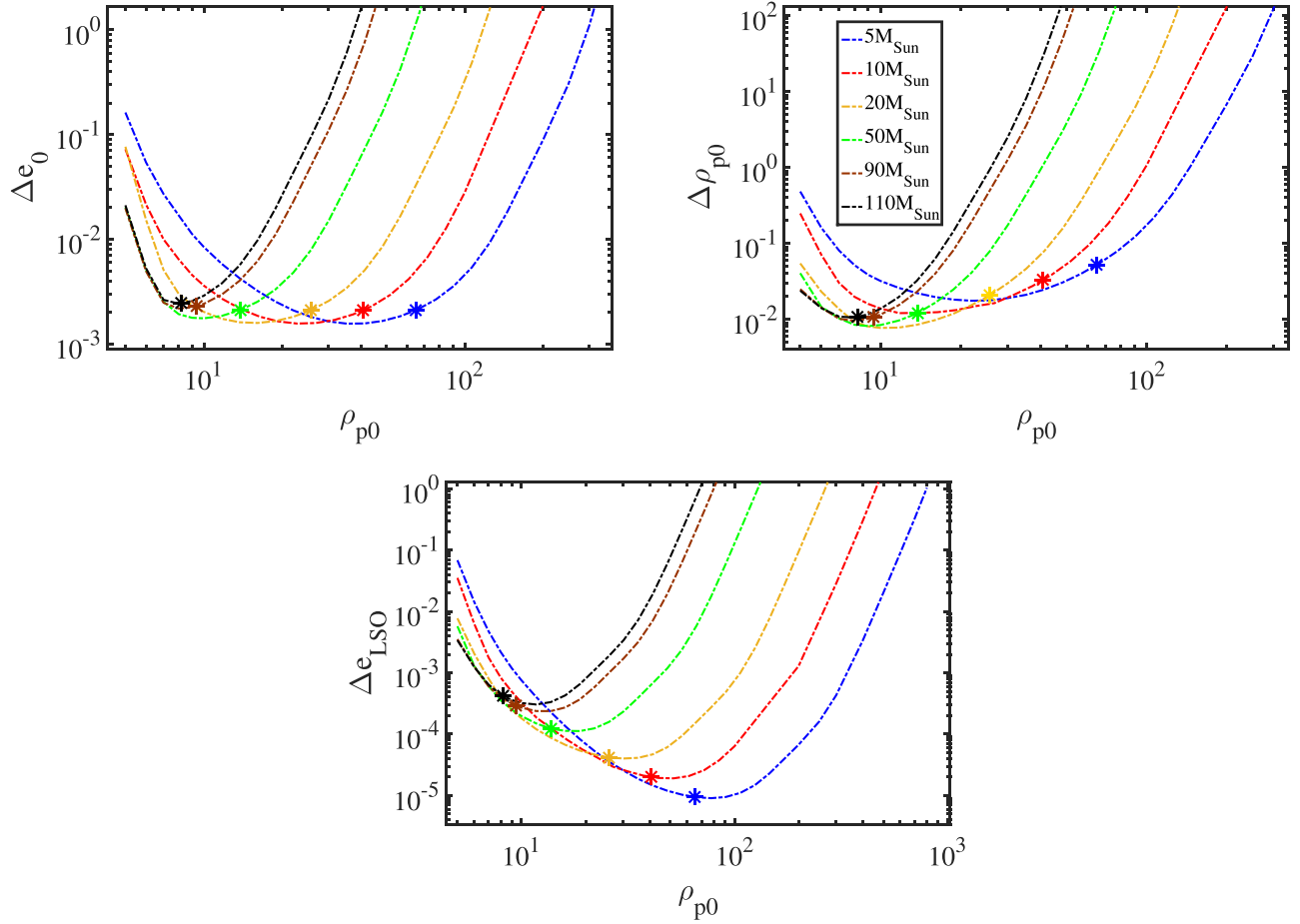
Figure 5. Same as Figure 3, but for precessing, eccentric, equal-mass BH–BH binaries with all binary parameters fixed as in the right panel of Figure 1. Binaries form in the detector's frequency band to the left of the stars.

$e_{10\,\mathrm{Hz}}$ to lower values. Asymptotically for $e_{10\,\mathrm{Hz}} < 0.04$, Figures 7 and 9 show that both Δe_{LSO} and $\Delta e_{10\,\mathrm{Hz}}$ can be fitted roughly with a power-law profile as $\Delta e_{\mathrm{LSO}} \propto e_{10\,\mathrm{Hz}}^{-\alpha_{\mathrm{LSO}}}$ and $\Delta e_{10\,\mathrm{Hz}} \propto e_{10\,\mathrm{Hz}}^{-\alpha_{10\,\mathrm{Hz}}}$, respectively, where the exponents are within the range $\alpha_{\mathrm{LSO}} \approx 4.7$–$5.3$ and $\alpha_{10\,\mathrm{Hz}} \approx 3.3$–$3.6$, depending on the component masses and the type of the binary.

5. Similar to $\Delta e_{10\,\mathrm{Hz}}$, the measurement error of the eccentricity at formation Δe_0 is lowest for binaries that form with $f_{\mathrm{GW}} \sim 10\,\mathrm{Hz}$, and somewhat worse for binaries that form well inside the band or enter the advanced GW detectors' frequency band with $e_{10\,\mathrm{Hz}} \lesssim e_0$ (Figures 3, 5, 7, and 9). For either precessing eccentric BH or NS binaries, the measurement error when the binary forms with $f_{\mathrm{GW}} \sim 10\,\mathrm{Hz}$ with $e_0 = e_{10\,\mathrm{Hz}} = 0.9$ is at the level of $\Delta e_0 \sim 10^{-3} \times (D_{\mathrm{L}}/100\,\mathrm{Mpc})$, which decreases to $\Delta e_0 \sim 10^{-1} \times (D_{\mathrm{L}}/100\,\mathrm{Mpc})$ when $e_{10\,\mathrm{Hz}} \sim 0.1$ or when binaries form with $\rho_{\mathrm{p0}} \lesssim 10$. Further, we find that Δe_0 has a weak mass dependence for binaries that enter the advanced GW detectors' frequency bands with similar $e_{10\,\mathrm{Hz}}$ values.

6. An important parameter that characterizes the velocity dispersion of the host environment or the orbital velocity of a binary before a hardening encounter is ρ_{p0} (O'Leary et al. 2009; Gondán et al. 2018b). This parameter can be measured at the level of $\Delta \rho_{\mathrm{p0}} \sim (10^{-2} - 10) \times (D_{\mathrm{L}}/100\,\mathrm{Mpc})$ for $e_{10\,\mathrm{Hz}} \gtrsim 0.1$, where the errors decrease with

increasing mass and $e_{10\,\mathrm{Hz}}$ (Figures 7 and 9). This parameter may be measured typically more accurately for binaries that form in the advanced GW detectors' frequency band than those that form outside of the bands (i.e., to the left of the stars in Figures 3 and 5) at the level of $\Delta \rho_{\mathrm{p0}} \sim (0.005\text{–}0.5) \times (D_{\mathrm{L}}/100\,\mathrm{Mpc})$.

3.3. Measurement Errors of Source Distance, Direction, Binary Orientation, and the Redshifted Chirp Mass

The measurement errors of source distance, sky location, and binary orientation (i.e., slow parameters) are lowest for binaries that form in the advanced GW detectors' frequency band (Figures 2 and 4), worse for binaries that enter the band with $e_{10\,\mathrm{Hz}} \lesssim e_0$ (Figures 6 and 8), and highest for binaries in the circular limit (i.e., $\rho_{\mathrm{p0}} \to \infty$ or equivalently $e_{10\,\mathrm{Hz}} \ll 1$). The measurement errors of these parameters slightly improve for precessing eccentric NS–NS, NS–BH, and BH–BH binaries forming in the band or entering the band with $e_{10\,\mathrm{Hz}} \lesssim e_0$ compared to similar binaries in the circular limit unless the BH masses exceed $\sim 50\,M_\odot$. This is expected because the measurement errors of slow parameters depend on the GW amplitude, which is set by the $\mathrm{S/N_{tot}}$ (Kocsis et al. 2007). Similar trends characterize the mass dependence of the $\mathrm{S/N_{tot}}$ (Figure 1). For BH masses in the range $50\,M_\odot$–$110\,M_\odot$, the measurement errors of slow parameters can improve by up to a factor of 2–4 and 2–20 for precessing eccentric NS–BH and
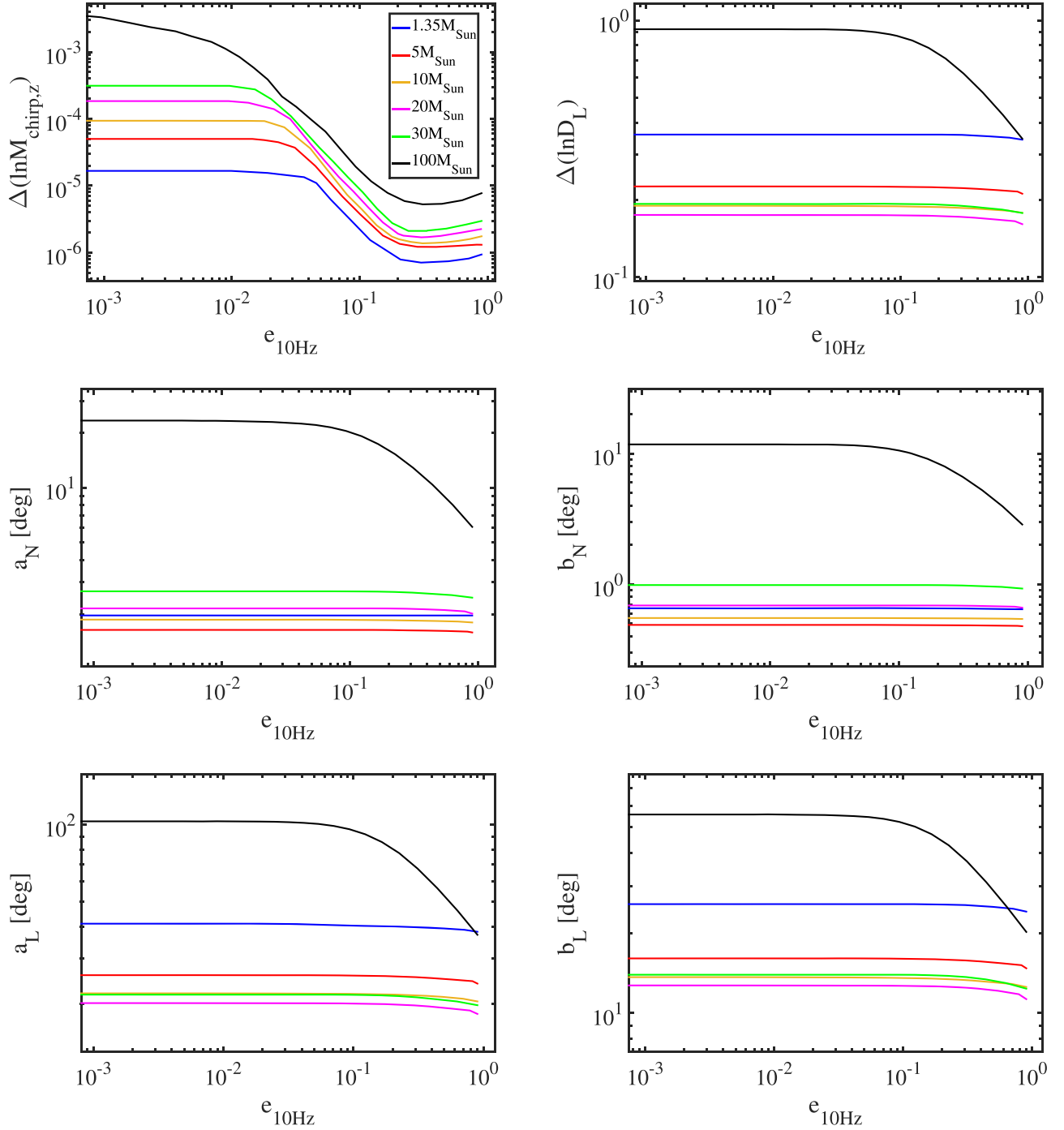
Figure 6. Measurement errors of source parameters for precessing eccentric NS–NS and NS–BH binaries as in Figure 2, but plotted as a function of $e_{10\,\mathrm{Hz}}$. Different curves show different companion masses as labeled in the legend.

BH–BH binaries, respectively, for $e_{10\,\mathrm{Hz}} \gtrsim 0.1$ compared to similar binaries in the circular limit. The errors improve systematically for higher $e_{10\,\mathrm{Hz}}$ values and for higher BH masses in the range $50\,M_\odot$–$110\,M_\odot$. For binaries that form in the advanced GW detectors' frequency band, the measurement precision further improves to factors of 2–6 and 2–50 for precessing eccentric NS–BH and BH–BH binaries, respectively.

The measurement error of redshifted chirp mass $\Delta(\ln \mathcal{M}_z)$ is lowest for binaries that form in the advanced GW detectors' frequency band near the detectors' low-frequency cutoff,

implying that they enter the band at $e_{10\,\mathrm{Hz}} \sim e_0$ (Figures 2 and 4). The measurement precision can improve by up to a factor of ~ 20 and ~ 50–100 for precessing eccentric NS–NS and NS–BH binaries with BH companion masses $\lesssim 40\,M_\odot$, respectively, compared to similar binaries in the circular limit. Even higher precision may be achieved for BH companion masses above $\sim 40\,M_\odot$, in particular, a factor of ~ 300 may be achieved for precessing eccentric NS–BH binaries with BH masses of $\sim 100\,M_\odot$ because for these sources a quasi-circular inspiral terminates outside of the frequency band. In comparison to circular binaries, the measurement accuracy can
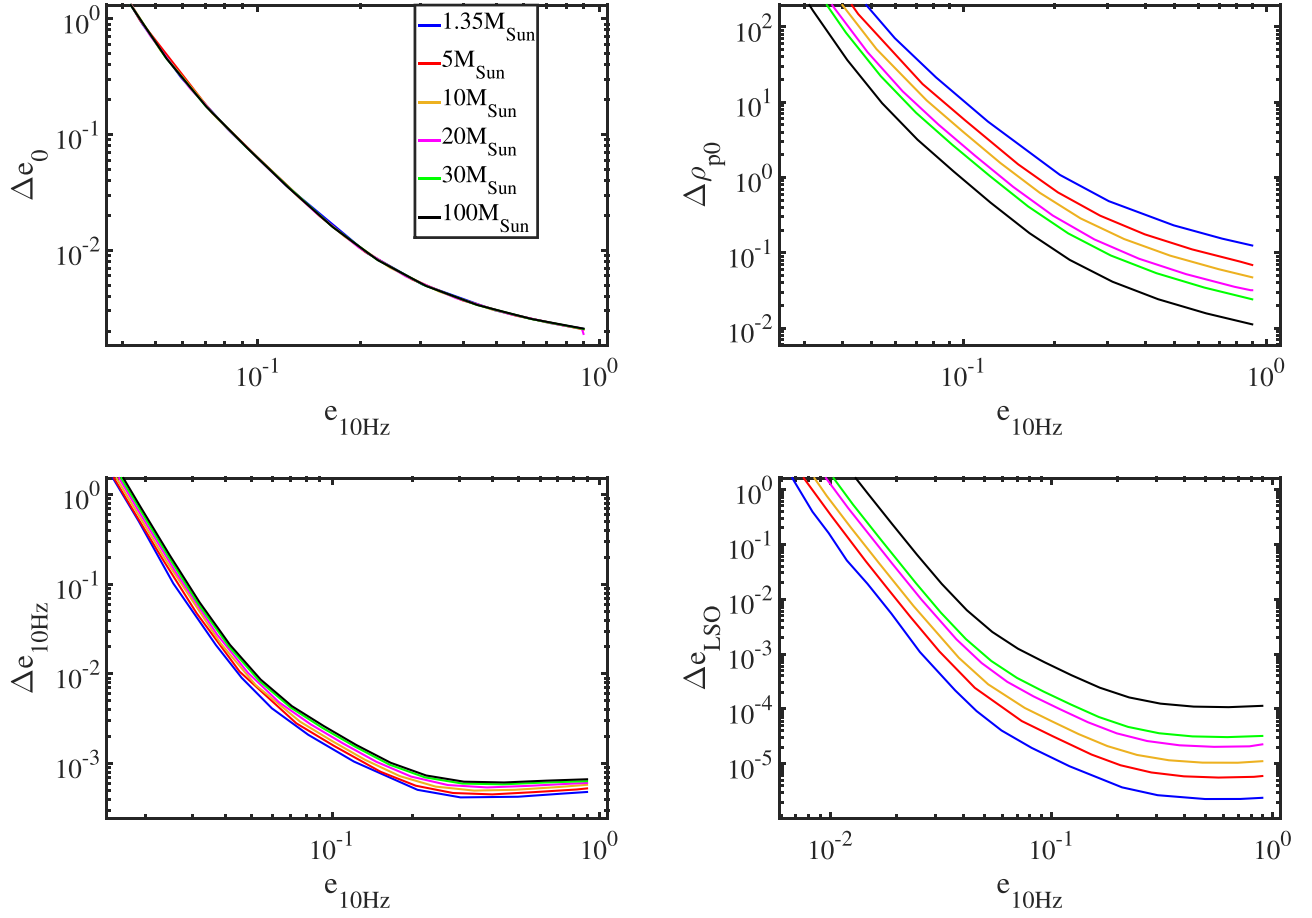
Figure 7. Measurement errors of source parameters specific for precessing eccentric NS–NS and NS–BH binaries as in Figure 3, plotted as a function of $e_{10\,\mathrm{Hz}}$ for binaries that form outside of the detectors' frequency band. Different curves show different companion masses as labeled in the legend.

improve by up to a factor of $\sim 10 - 10^2$ and $\sim 10^2$–10^3 for precessing eccentric BH–BH binaries with BH masses below $\sim 40\,M_\odot$ and BH masses in the range $40 - 110\,M_\odot$, respectively. In all cases, higher precision corresponds to higher $e_{10\,\mathrm{Hz}}$ values and BH masses.

We find in agreement with O'Leary et al. (2009) that the $\mathrm{S/N_{tot}}$ can be significantly greater for high-mass binaries with relatively low ρ_{p0} than for similar binaries in the circular limit, which implies that eccentric binaries with higher masses may be detected to larger distances, and generally greater BH mass binaries may be detected if eccentric than similar binaries in the circular mergers; see Figure 1 for examples. Similarly, we find that measurement errors of slow binary parameters are comparable for low-mass and high-mass precessing eccentric BH–BH binaries and for precessing eccentric NS–BH binaries with BH companion masses $\lesssim 30\,M_\odot$ when binaries form in the advanced GW detectors' frequency band (Figures 2 and 4) or enter the 10 Hz frequency band with $0.1 \lesssim e_{10\,\mathrm{Hz}}$ and $e_{10\,\mathrm{Hz}} \leqslant e_0$, respectively (Figures 6 and 8).

3.4. Measurement Accuracy of the Characteristic Relative Velocity

For GW capture events with a fixed v initial relative velocity between two compact objects, the initial pericenter distance ρ_{p0} is uniformly distributed up to a critical value where the system forms a marginally bound binary (Kocsis et al. 2006; O'Leary et al. 2009; Gondán et al. 2018b). Similarly, for resonant binary–single encounters (Rodriguez et al. 2018a, 2018b;

Samsing 2018), the GW emission may form a merging binary whose ρ_{p0} is expected to be approximately uniformly distributed up to a critical value set by the orbital velocity before a hardening encounter plus the initial velocity of the scattering object. A crude relation between the initial pericenter distance and the orbital velocity of the binary may be derived from Equation (18) in O'Leary et al. (2009),

$$\rho_{p0} \sim \left(\frac{85\pi\eta}{6\sqrt{2}}\right)^{2/7} v_{\mathrm{bin}}^{-4/7} = 175\,(4\eta)^{2/7}\left(\frac{v_{\mathrm{bin}}}{100\,\mathrm{km\,s^{-1}}}\right)^{-4/7},$$

(12)

where the symmetric mass ratio η is defined above in Equation (11). Here v_{bin} can be expressed by the measurable quantities η and ρ_{p0} as

$$v_{\mathrm{bin}} \sim 266\,\mathrm{km\,s^{-1}} \times (4\eta)^{1/2}\left(\frac{\rho_{p0}}{100}\right)^{-7/4}.$$

(13)

The initial pericenter distance ρ_{p0} sets the eccentricity at the LSO (see Equations (30) and (32) in Gondán et al. 2018b).

Similar arguments apply for single–single GW capture sources in GNs and GCs, where v_{bin} is replaced by $2\sqrt{2}\,\sigma$,[15] where σ refers to the characteristic velocity dispersion of the

---

[15] For single–single GW capture sources, ρ_{p0} depends on the maximum relative velocity between the objects in Equation (12), which is $v_{\mathrm{rel,max}} = 2v_{\mathrm{max}}$, where v_{max} is the maximum velocity of the individual objects in the system. Given the velocity dispersion, this may be expressed as $\sigma \sim v_{\mathrm{max}}/\sqrt{2}$.
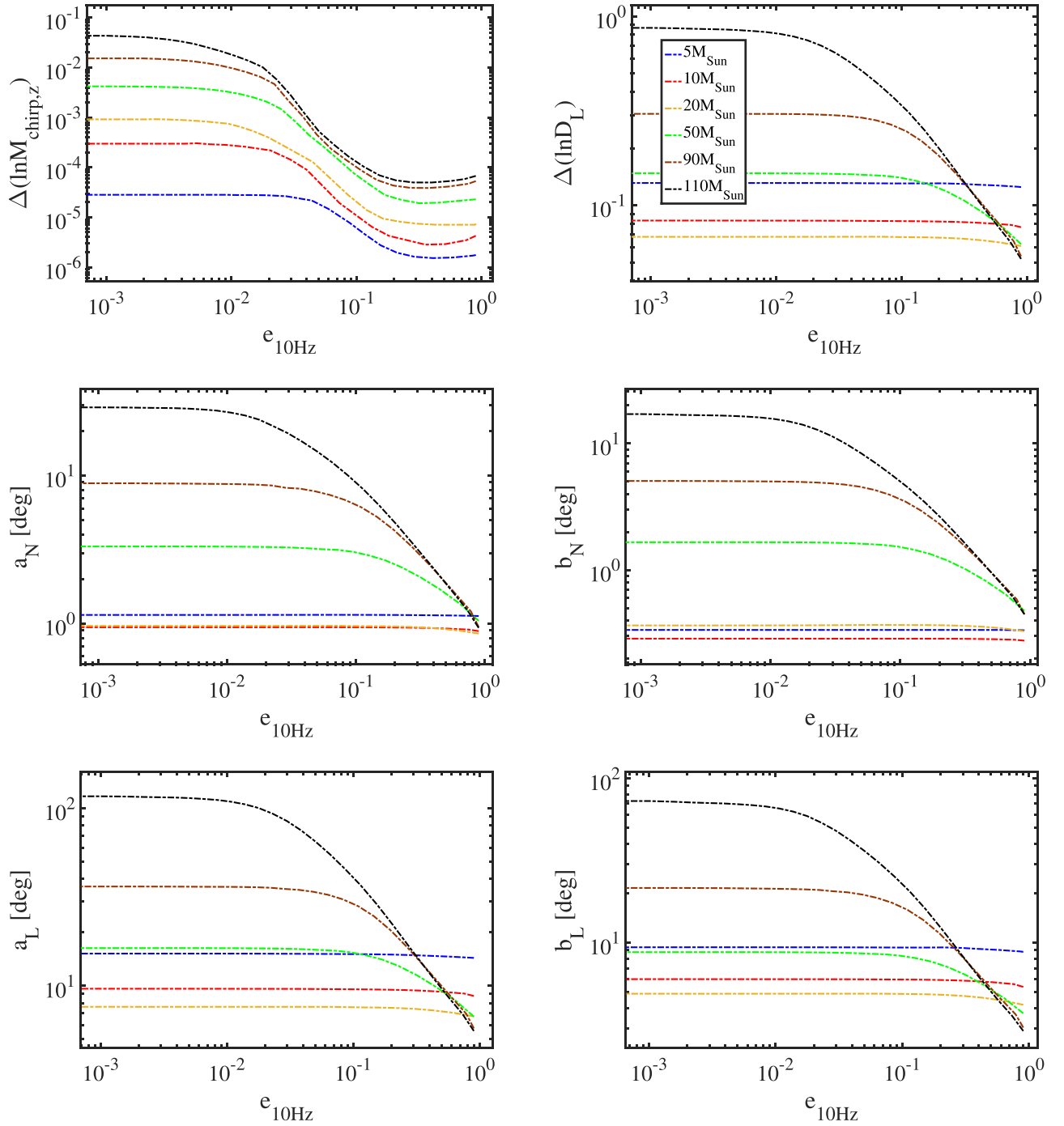
Figure 8. Same as Figure 6, but for precessing, eccentric, equal-mass BH–BH binaries of different masses, showing binaries that form outside of the detectors' frequency band.

host environment (Gondán et al. 2018b). Thus, σ[16] can be expressed by η and ρ_{p0} as

$$\sigma \sim 94 \text{ km s}^{-1} \times (4\eta)^{1/2} \left(\frac{\rho_{p0}}{100}\right)^{-7/4}. \quad (15)$$

---

[16] Note that Equation (63) in Gondán et al. (2018b) relates the eccentricity at the LSO to σ as

$$\sigma \sim 258 \text{ km s}^{-1} \times (4\eta)^{1/2} \left(\frac{e_{\text{LSO}}}{0.01}\right)^{35/32}, \quad (14)$$

which can be given by substituting ρ_{p0} with e_{LSO} in Equation (15) using Equation (32) in Gondán et al. (2018b).

From Equation (13) and using Equations (1) and (2), the measurement error of $v_{\text{bin}} = v_{\text{bin}}(\eta, \rho_{p0})$ can be expressed as

$$(\Delta v_{\text{bin}})^2 = \left(\frac{\partial v_{\text{bin}}(\eta, \rho_{p0})}{\partial \eta}\right)^2 (\Delta \eta)^2$$

$$+ \left(\frac{\partial v_{\text{bin}}(\eta, \rho_{p0})}{\partial \rho_{p0}}\right)^2 (\Delta \rho_{p0})^2$$

$$+ 2 \frac{\partial v_{\text{bin}}(\eta, \rho_{p0})}{\partial \eta} \frac{\partial v_{\text{bin}}(\eta, \rho_{p0})}{\partial \rho_{p0}} \langle \Delta \eta \Delta \rho_{p0} \rangle, \quad (16)$$
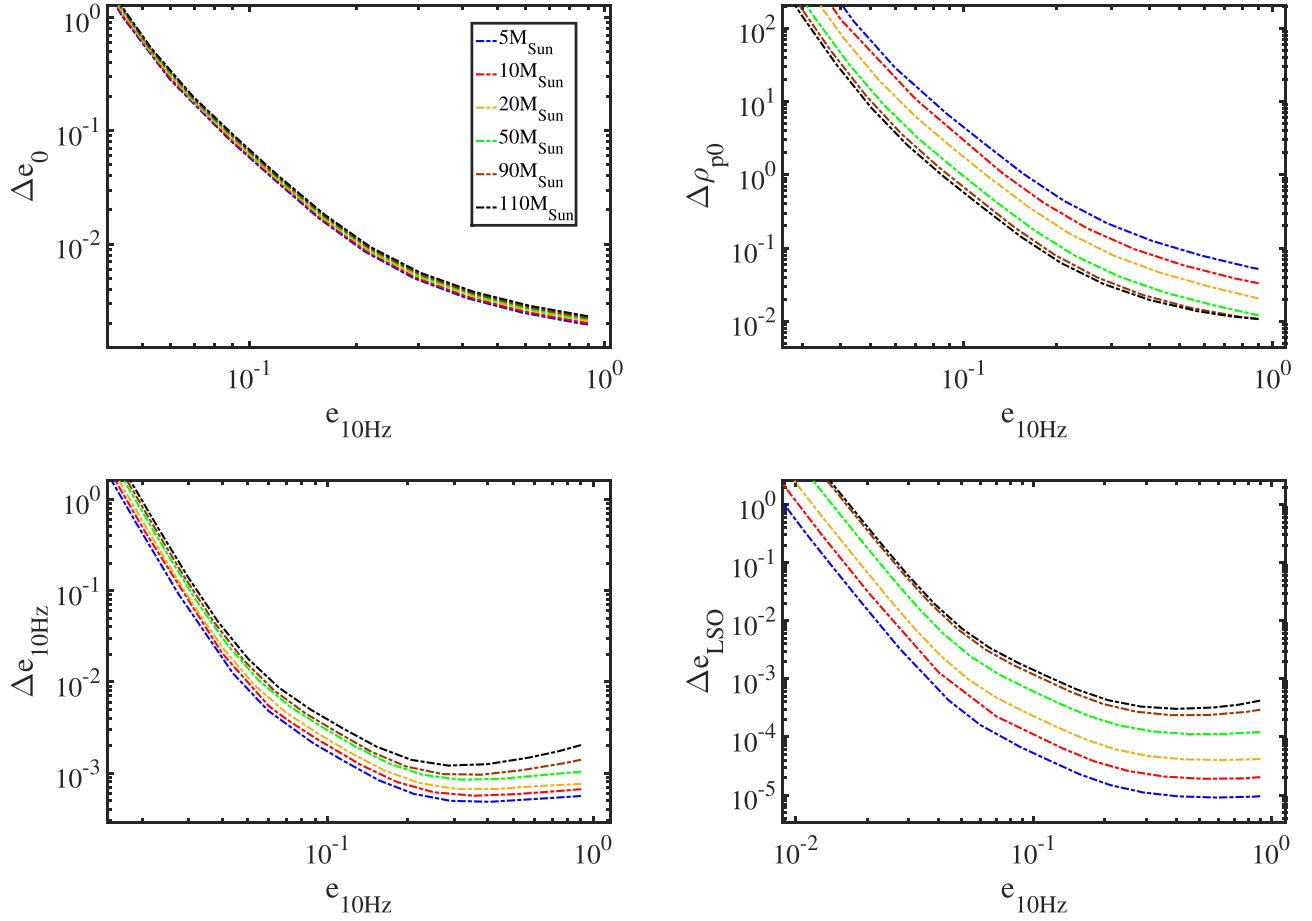
Figure 9. Same as Figure 7, but for precessing, eccentric, equal-mass BH–BH binaries.

which simplifies as

$$\frac{\Delta v_{\mathrm{bin}}}{v_{\mathrm{bin}}} = \sqrt{\left(\frac{1}{2}\right)^2 \frac{(\Delta \eta)^2}{\eta^2} + \left(\frac{7}{4}\right)^2 \frac{(\Delta \rho_{\mathrm{p0}})^2}{\rho_{\mathrm{p0}}^2}}, \qquad (17)$$

and an identical equation holds for $\Delta \sigma / \sigma$. Here we used the fact that the cross-correlation coefficient $\langle \Delta \eta \Delta \rho_{\mathrm{p0}} \rangle$ is negligible compared to $(\Delta \eta)^2$ and $(\Delta \rho_{\mathrm{p0}})^2$, as found from numerical investigations. $\Delta \eta / \eta$ can be given using Equation (54) in Gondán et al. (2018a), and we find from numerical investigation that crudely $\Delta \eta / \eta \sim 10 \, \Delta \mathcal{M}_z / \mathcal{M}_z$; see Table 4 in Gondán et al. (2018a) for examples. Thus, since $\Delta v_{\mathrm{bin}} / v_{\mathrm{bin}} = \Delta \sigma / \sigma$, we refer to both v_{bin} and σ as the "characteristic relative velocity" w and denote $\Delta v_{\mathrm{bin}} / v_{\mathrm{bin}}$ and $\Delta \sigma / \sigma$ by $\Delta w / w$ in this paper.

Results for $\Delta w / w$ are displayed in Figure 10. Generally, $\Delta w / w$ is at the level of $\Delta w / w \sim (10^{-3}\text{--}10^{-1}) \times (D_{\mathrm{L}}/$ 100 Mpc) for $0.04 \lesssim e_{10\,\mathrm{Hz}}$, where lower errors correspond to higher $e_{10\,\mathrm{Hz}}$ values. In particular, $\Delta w / w$ is lowest for binaries that form in the advanced GW detectors' frequency band near the low-frequency cutoff of detectors or enter the band at $e_{10\,\mathrm{Hz}} \sim e_0$, and it is higher for binaries that form well inside the band or form with $e_{10\,\mathrm{Hz}} < e_0$. Further, we find that $\Delta w / w$ weakly depends on the binary mass for different $e_{10\,\mathrm{Hz}}$ values for all types of binaries. We conclude that the characteristic relative velocity can be estimated with high accuracy with GW observations of eccentric mergers.

3.5. Initial Orbital Parameter Dependence of Measurement Errors

We identify the following trends for the ρ_{p0} dependence of measurement errors in Figures 1–5.

1. The ρ_{p0} dependence of the slow parameter errors ($\Delta \ln D_L$, a_N, b_N, a_L, b_L) is qualitatively similar to that of $1/(\mathrm{S/N_{tot}})$, as expected (Kocsis et al. 2007). The errors have a minimum at moderate ρ_{p0} between 10 and 100. The errors increase rapidly with decreasing ρ_{p0} for lower ρ_{p0}, and converge asymptotically for ρ_{p0} to the value of the circular limit.

2. The measurement errors of fast parameters (Equation 3) are qualitatively similar to those of slow parameters (Equation 4) in terms of their ρ_{p0} dependence, except that they have a minimum at a higher ρ_{p0}, which corresponds to a characteristic GW frequency of $f_{\mathrm{GW}} \sim 7$ Hz. Further, Δe_{LSO} is inaccurately estimated by our method for high ρ_{p0} as the Fisher matrix algorithm becomes invalid in that regime.

3. The initial parameters Δe_0 and $\Delta \rho_{\mathrm{p0}}$ increase rapidly with ρ_{p0} for high ρ_{p0} and become indeterminate in the circular limit. Indeed, for high ρ_{p0}, the binary forms outside of the advanced GW detectors' frequency band, and the measured GW signal cannot specify the initial condition. Similarly, Δe_0 and $\Delta \rho_{\mathrm{p0}}$ increase rapidly in the limit of low ρ_{p0} because of a low $\mathrm{S/N_{tot}}$ and possible degeneracies among the parameters.
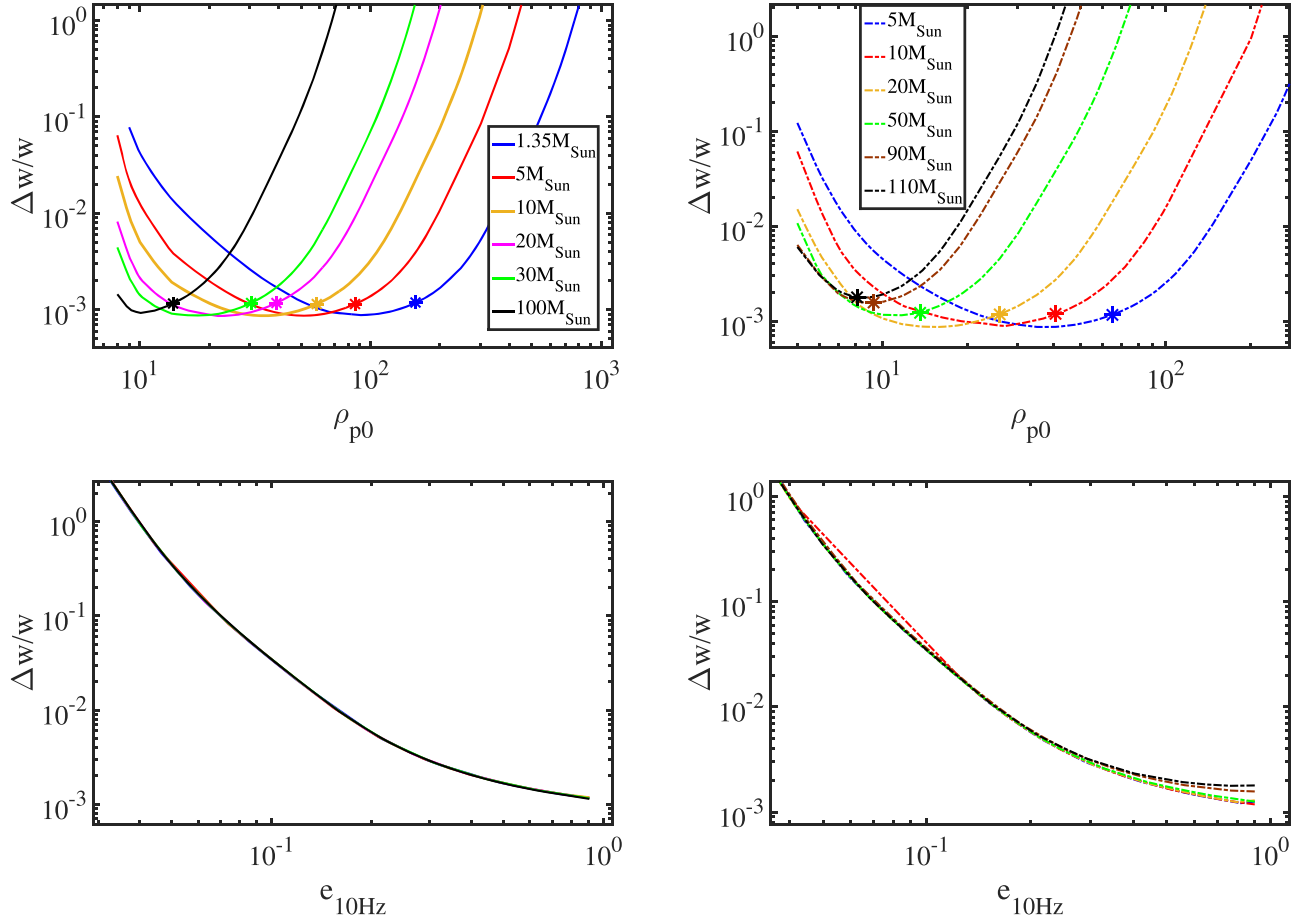
Figure 10. Measurement accuracy of the characteristic relative velocity of the sources before GWs start driving the evolution for precessing eccentric NS–NS and NS–BH binaries (left) and for precessing eccentric BH–BH binaries (right) as a function of ρ_{p0} (top) and $e_{10\,\mathrm{Hz}}$ (bottom). This is expected to be comparable to the velocity dispersion of the host environment. Measurement errors are calculated by combining the chirp mass errors with the e_{LSO} errors as in Equation (17). Different curves show different companion masses as labeled in the legends. Parameters of the detector network and all other binary parameters are fixed as in Figure 1. Similar to Figures 2 and 3, measurement errors are displayed for 100 Mpc, but can be scaled to other D_L values by multiplying the displayed results by a factor of $D_L/100$ Mpc. Stars indicate the case where the binary forms at $f_{\mathrm{GW}} = 10$ Hz as in Figure 1. We find similar trends with ρ_{p0} and $e_{10\mathrm{Hz}}$ for other random choices of binary direction and orientation (not shown).

We refer the readers for further discussion to Gondán et al. (2018a).

Furthermore, we find that measurement accuracies do not improve significantly for the parameter ranges shown in Figures 1–5 if e_0 is increased beyond $e_0 \sim 0.9$. For instance, measurement accuracies of fast parameters (Equation 3), slow parameters (Equation 4), the parameters (e_0, ρ_{p0}), and $e_{10\,\mathrm{Hz}}$ improve by up to a factor of ~ 2, ~ 1.1, ~ 2, and ~ 2, respectively, if e_0 is increased from 0.9 to 0.99.

3.6. Mass Dependence of Measurement Errors

The mass dependence of the measurement accuracies can be examined by comparing the different curves in Figures 2–9. This shows that $(\Delta \ln D_L, a_N, b_N, a_L, b_L)$ have a minimum as a function of mass for fixed ρ_{p0}. The mass dependency of $(\Delta \ln D_L, a_N, b_N, a_L, b_L)$ can be understood from the scaling $1/(S/N_{\mathrm{tot}})$, which has a maximum at fixed ρ_{p0} (O'Leary et al. 2009). The characteristic GW spectral amplitude per logarithmic frequency bin (i.e $h_{\mathrm{char}} = f\tilde{h} \propto \mathcal{M}^{5/6} f^{-1/6}$) is an increasing function of the total binary mass and is roughly independent of frequency for frequencies lower than the ISCO

$f_{\mathrm{ISCO}} \propto M_{\mathrm{tot},z}^{-1}$. The detector noise per logarithmic frequency bin increases for lower frequencies. The combination of these effects is to increase/decrease the S/N_{tot} for total masses lower/higher than roughly $50 M_\odot$ for low-eccentricity or circular binaries. The total binary mass at which the S/N_{tot} peaks $M_{\mathrm{tot},z,\mathrm{peak}}$ depends on ρ_{p0}; see Figure 11 in O'Leary et al. (2009) for an example. Additionally, $S/N_{\mathrm{tot}} \propto \eta^{1/2}$ at fixed $M_{\mathrm{tot},z}$, which implies that the slow parameter errors are proportional to $\eta^{-1/2}$ so that nearly equal-mass binaries are localized better than unequal-mass binaries. There are small differences with respect to the $(S/N_{\mathrm{tot}})^{-1}$ scaling for $\Delta \ln D_L$, (a_N, b_N), and (a_L, b_L), respectively, as the S/N_{tot} is the scalar product of the waveform with itself, while $\ln D_L$, (θ_N, ϕ_N), and (θ_L, ϕ_L) are set by the inverse of the Fisher matrix, which have elements given by the scalar product of the parameter derivatives of the waveform. The nonzero correlation between these slow parameters and the masses introduces small differences in the mass dependences of the inverse matrix elements (see Sections 4 and 5 in Gondán et al. 2018a).

The measurement errors of fast parameters (e.g., $\ln \mathcal{M}_z$ and e_{LSO}) and $(e_0, e_{10\,\mathrm{Hz}})$ increase with the binary mass because a higher amount of GW phase accumulates in the detector band for
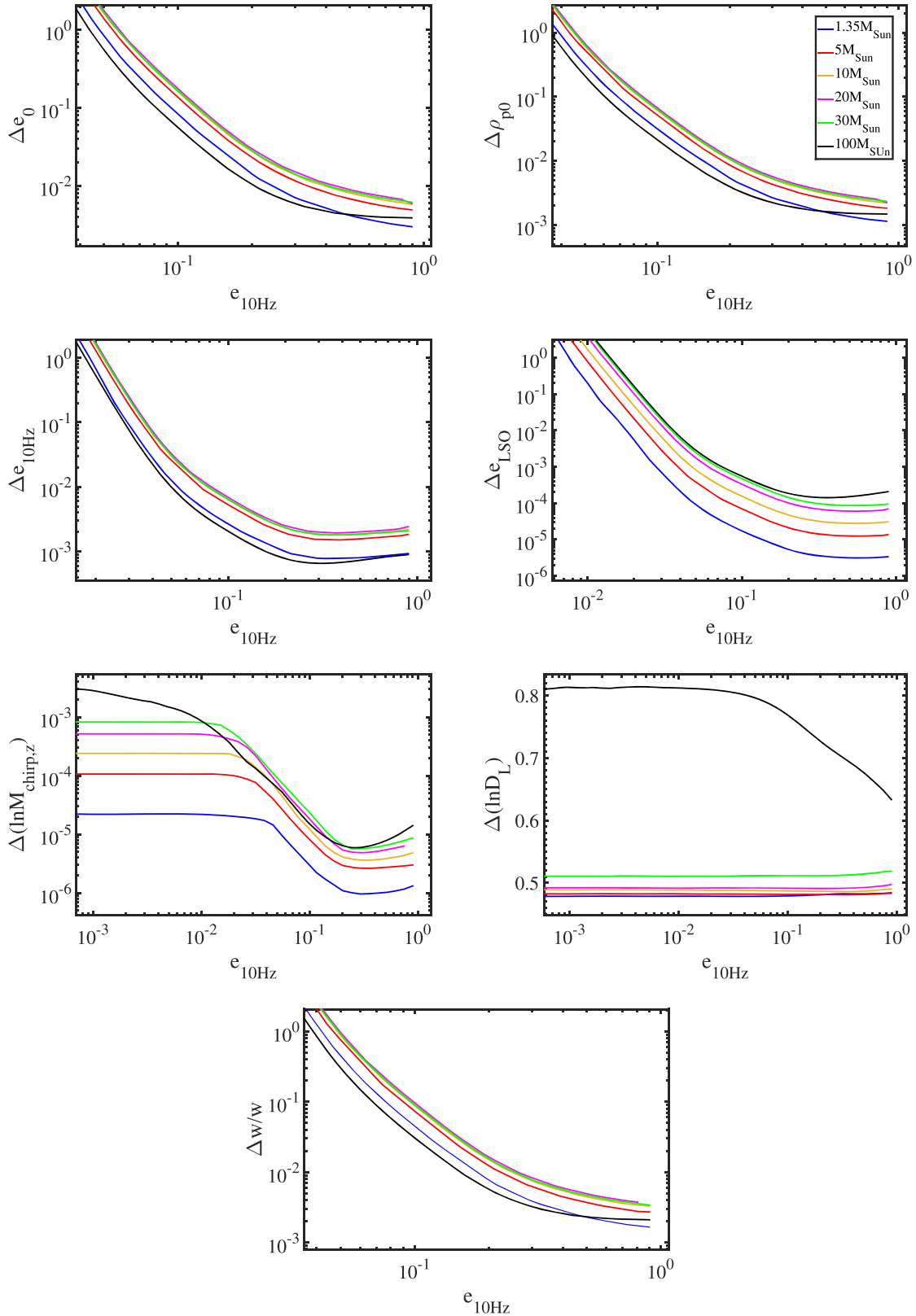
Figure 11. Measurement errors of various source parameters as a function of $e_{10\mathrm{Hz}}$ for precessing eccentric NS–NS and NS–BH binaries with different companion masses as labeled in the legend, showing binaries that form outside of the detectors' frequency band. Results are displayed for a reference S/N_{tot} of 20, but can be scaled to other S/N_{tot} values by multiplying the displayed results by a factor of $20 \times (S/N_{\mathrm{tot}})^{-1}$. Parameters of the detector network and all other binary parameters are fixed as in Figure 1. First row left: Initial eccentricity Δe_0. First row right: Initial dimensionless pericenter distance $\Delta \rho_{p0}$. Second row left: Eccentricity at a GW frequency of 10 Hz $\Delta e_{10\mathrm{Hz}}$. Second row right: Eccentricity at the LSO Δe_{LSO}. Third row left: Redshifted chirp mass, $\Delta \mathcal{M}_z / \mathcal{M}_z = \Delta(\ln \mathcal{M}_z)$. Third row right: Luminosity distance $\Delta D_L / D_L = \Delta(\ln D_L)$. Fourth row: Characteristic relative velocity $\Delta w/w$. We find similar trends with $e_{10\mathrm{Hz}}$ for other random choices of binary direction and orientation (not shown).
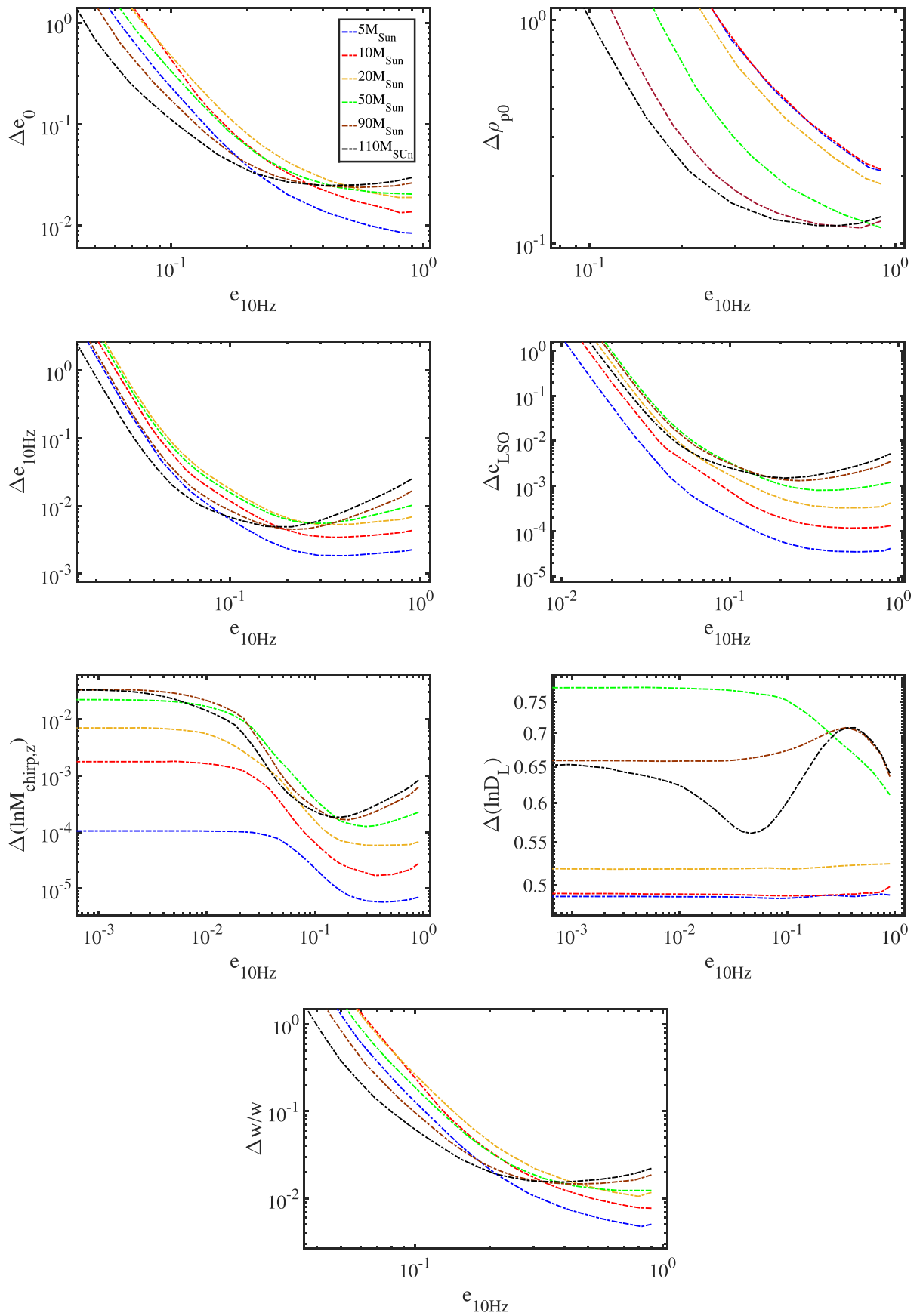
Figure 12. Same as Figure 11, but for precessing, eccentric, equal-mass BH–BH binaries of different masses, showing binaries that form outside of the detectors' frequency band.

lower binary mass. Indeed, the frequency-dependent GW phase is proportional to $\mathcal{M}^{-5/3}$ at leading order (Cutler & Flanagan 1994), and the effect of pericenter precession does not modify this dependence significantly.

We compare our results with a previous study of Ajith & Bose (2009) for the M_{tot} dependence of $\Delta(\ln D_L)$ and $\Delta(\ln \mathcal{M}_z)$ (i.e., for the mutual parameters) for fixed D_L in the circular limit. We find that $\Delta(\ln D_L)$ has one global minimum for a certain M_{tot} value[17] and $\Delta(\ln \mathcal{M}_z)$ systematically increases with M_{tot} (Figures 2 and 4). These findings are qualitatively in agreement with results presented for the considered waveform model in the inspiral phase in Figures 2–4 in Ajith & Bose (2009).[18]

3.7. Measurement Errors of Binary Parameters as a Function of $e_{10\,Hz}$ for Fixed S/N_{tot}

In Figures 11 and 12, we scale the $e_{10\,Hz}$ dependent measurement errors of binary parameters (e_0, ρ_{p0}, $\ln \mathcal{M}_z$, $\ln D_L$, $\ln w$, $e_{10\,Hz}$, e_{LSO}) to $S/N_{tot} = 20$, and show results for binaries that form outside of the detectors' frequency band. Fixing the S/N_{tot} eliminates the observational selection bias from the detection likelihood. For a homogeneous isotropic source population in Euclidian space, the number of events with a given S/N_{tot} value is approximately proportional to $(S/N_{tot})^{-4}$. Thus, the parameter dependence of the measurement precision shown in Figures 11 and 12 for fixed S/N_{tot} represents the relative number of sources with different measurement accuracies in a magnitude-limited sample.

To obtain these figures, note that in Appendix B we show that measurement errors and S/N_{tot} scale roughly as $\propto D_L$ and $\propto 1/D_L$, respectively, implying that $\Delta\lambda \propto (S/N_{tot})^{-1}$. Thus, the measurement errors can be given for $S/N_{tot} = 20$ by the product $\Delta\lambda(e_{10\,Hz}) \times [S/N_{tot}(e_{10\,Hz})/20]$, where both $\Delta\lambda(e_{10\,Hz})$ and S/N_{tot} are calculated for $D_L = 100$ Mpc. Further, we note that measurement errors can be scaled to other S/N_{tot} values by multiplying the displayed results by a factor of $20 \times (S/N_{tot})^{-1}$. Results for an S/N_{tot} of 20 are displayed in Figures 11 and 12.

For fixed S/N_{tot}, the mass and $e_{10\,Hz}$ dependent trends of measurement errors vary relative to that for fixed D_L as follows: For precessing eccentric NS–BH and BH–BH binaries with BH masses $\lesssim 30 M_{\odot}$, the S/N_{tot} is nearly constant (increases weakly) as a function of $e_{10\,Hz}$ (Figure 1), consequently, the $e_{10\,Hz}$ dependent trends of measurement errors are similar for fixed S/N_{tot} or for fixed D_L. However, for precessing eccentric NS–BH and BH–BH binaries with BH masses $\lesssim 30 M_{\odot}$, these trends change significantly depending on the type of binary and the parameter; see errors for $\ln D_L$ for BH–BH binaries in Figure 12 as an example.

We identify the following trends. Note that many of these statements are nearly identical to those made earlier for fixed D_L.

1. The measurement error of $e_{10\,Hz}$ is in the range $\Delta e_{10\,Hz} \sim (10^{-3} - 10^{-2}) \times 20 \times (S/N_{tot})^{-1}$ for precessing eccentric NS–NS, NS–BH, and BH–BH binaries if $e_{10\,Hz} > 0.1$.

2. Δe_{LSO} is at the level of $\Delta e_{LSO} \sim (10^{-3} - 10^{-5}) \times 20 \times (S/N_{tot})^{-1}$ for precessing eccentric NS–BH and BH–BH binaries if $e_{10\,Hz} > 0.1$, while measurement errors for precessing eccentric NS–NS binaries are in the range $\Delta e_{LSO} \sim (10^{-6} - 10^{-5}) \times 20 \times (S/N_{tot})^{-1}$.

3. The measurement error of e_0 is at the level of $\Delta e_0 \sim (10^{-3} - 10^{-1}) \times 20 \times (S/N_{tot})^{-1}$ for precessing eccentric NS–NS, NS–BH, and BH–BH binaries if $e_{10\,Hz} \gtrsim 0.1$, where errors systematically decrease with $e_{10\,Hz}$ for NS–NS and NS–BH binaries and for BH–BH binaries with BH masses $\lesssim 30 M_{\odot}$.

4. ρ_{p0} can be measured at the level of $\Delta\rho_{p0} \sim (10^{-3} - 10^{-1}) \times 20 \times (S/N_{tot})^{-1}$ for precessing eccentric NS–NS and NS–BH binaries if $e_{10\,Hz} \gtrsim 0.1$, where the errors decrease with $e_{10\,Hz}$. $\Delta\rho_{p0}$ is in the range $10^{-1} \times 20 \times (S/N_{tot})^{-1}$ and $(10^{-1} - 10) \times 20 \times (S/N_{tot})^{-1}$ for precessing eccentric BH–BH binaries with BH masses $\lesssim 90 M_{\odot}$ and $90 M_{\odot} \lesssim$, respectively.

5. In comparision to circular binaries, the measurement error of source distance, sky location, and binary orientation slightly improves/deteriorates for precessing eccentric NS–NS, NS–BH, and BH–BH binaries.

6. The measurement accuracy of $\mathcal{M}_z$ can improve by up to a factor of ~ 20 and ~ 30–100 for precessing eccentric NS–NS and NS–BH binaries with BH companion masses $\lesssim 40 M_{\odot}$, respectively, compared to similar binaries in the circular limit. Even higher precision may be achieved for BH companion masses above $\sim 40 M_{\odot}$, in particular, a factor of ~ 200 may be achieved for NS–BH binaries with BH masses of $\sim 100 M_{\odot}$. In comparison to circular binaries, the measurement accuracy improves by up to a factor of ~ 10–10^2 and 100–150 for precessing eccentric BH–BH binaries with BH masses below and above $\sim 40 M_{\odot}$, respectively.

7. The measurement accuracy of the characteristic relative velocity is in the range $\Delta w/w \sim (10^{-3} - 10^{-1}) \times 20 \times (S/N_{tot})^{-1}$ for precessing eccentric NS–NS, NS–BH, and BH–BH binaries if $e_{10\,Hz} \gtrsim 0.1$, where higher precision corresponds to higher $e_{10\,Hz}$ values. Further, errors systematically decrease with $e_{10\,Hz}$ for NS–NS and NS–BH binaries and for BH–BH binaries with BH masses $\lesssim 30 M_{\odot}$.

Finally, we compare our results with those of Ajith & Bose (2009) for the M_{tot} dependence of $\Delta(\ln D_L)$ and $\Delta(\ln \mathcal{M}_z)$ (i.e., for the mutual parameters) for fixed S/N_{tot} in the circular limit. We find for NS–NS and NS–BH binaries that $\Delta(\ln D_L)$ slightly increases below a certain M_{tot} value, but rapidly increases above it and $\Delta(\ln \mathcal{M}_z)$ systematically increases with M_{tot} (Figures 11 and 12), which qualitatively agrees with results presented for the considered waveform model in the inspiral phase in Figures 6–8 in Ajith & Bose (2009). We find similar trends for BH–BH binaries with $M_{tot} \lesssim 130 M_{\odot}$, but these trends break for $M_{tot} \gtrsim 130 M_{\odot}$ because the M_{tot} dependence of the S/N_{tot} decreases more rapidly above $M_{tot} \sim 130 M_{\odot}$ for the considered waveform model (Section 2.1) in the circular limit than in the inspiral phase in Ajith & Bose (2009).

4. Discussion and Conclusion

In this paper, we have carried out a Fisher matrix type analysis to estimate the expected measurement errors of the

---

[17] We find this global minimum to be between $50 M_{\odot}$ and $60 M_{\odot}$ for the aLIGO–AdV–KAGRA detector network at design sensitivity.

[18] Note that only a qualitative comparison is possible because Ajith & Bose (2009) considered different detectors with noise curves and applied different waveform models.

physical parameters characterizing non-spinning precessing eccentric binary inspirals with the aLIGO–AdV–KAGRA GW detector network. We carried out calculations for compact object masses that correspond to precessing eccentric NS–NS, NS–BH, and BH–BH binaries with BH masses in the range $5\,M_\odot - 110\,M_\odot$ and a wide range of dimensionless initial pericenter distances ρ_{p0} to cover binaries that form in the advanced GW detectors' frequency band with high eccentricities to those that enter it at 10 Hz with eccentricities between $8 \times 10^{-4} \leqslant e_{10\,\mathrm{Hz}} \leqslant 0.9$.

The results show that the source distance, sky location, and binary orientation parameter measurement precision (the so-called slow parameters; Kocsis et al. 2007) are roughly independent of $e_{10\,\mathrm{Hz}}$ for precessing eccentric NS–NS and NS–BH binaries unless the BH companion mass is higher than $\sim 50\,M_\odot$. The distance, source sky location, and binary orientation measurement precision improve significantly by a factor of 2–20 for $e_{10\,\mathrm{Hz}} \gtrsim 0.1$ for precessing eccentric NS–BH and BH–BH binaries with BH masses in the range $50\,M_\odot - 110\,M_\odot$ compared to similar binaries in the circular limit, where higher accuracies correspond to higher $e_{10\,\mathrm{Hz}}$ values and binary masses. The measurement precision further improves to 2–50 when these binaries form in the advanced GW detectors' frequency band.

The measurement accuracy of the characteristic relative velocity is in the range $\Delta w/w \sim (10^{-3} - 10^{-1}) \times (D_L/100\,\mathrm{Mpc})$ for $0.04 \lesssim e_{10\,\mathrm{Hz}}$, where lower errors correspond to higher $e_{10\,\mathrm{Hz}}$ values, and results weakly depend on the binary mass. The relative velocity is expected to be a proxy for the velocity dispersion of the host environment or it may estimate the initial orbital velocity of the binary in a single-binary resonant scattering encounter.

The measurement accuracy of other parameters such as $\mathcal{M}_z$, ρ_{p0}, e_0, $e_{10\,\mathrm{Hz}}$, and e_{LSO} are sensitive to the eccentricity for all component masses.

$\mathcal{M}_z$ is expected to be measured to a much higher measurement accuracy for more eccentric precessing NS–NS, NS–BH, and BH–BH sources with $e_{10\,\mathrm{Hz}} \gtrsim 0.1$ than for similar binaries in the circular limit. The improvement is by a factor of $\sim 10 - 10^3$, where higher accuracies correspond to higher masses and $e_{10\,\mathrm{Hz}}$ values.

The eccentricity measurement errors at a GW frequency of 10 Hz and at the LSO are in the range $\Delta e_{10\,\mathrm{Hz}} \sim (10^{-4} - 10^{-3}) \times (D_L/100\,\mathrm{Mpc})$ and $\Delta e_{\mathrm{LSO}} \sim (10^{-6} - 10^{-3}) \times (D_L/100\,\mathrm{Mpc})$, respectively, for precessing eccentric NS–NS, NS–BH, and BH–BH binaries if $e_{10\,\mathrm{Hz}} \gtrsim 0.1$, where lower errors correspond to lower masses and higher $e_{10\,\mathrm{Hz}}$ values. Further, we showed that $e_{10\,\mathrm{Hz}}$ can be measured effectively for the GW transients analogous to GW150914, GW151226, GW170104, GW170608, GW170729, GW170809, GW170814, GW170817, GW170818, and GW170823 if $e_{10\,\mathrm{Hz}} \gtrsim \{0.051, 0.046, 0.058, 0.043, 0.081, 0.063, 0.053, 0.023, 0.062, 0.072\}$, respectively.

The initial[19] eccentricity and pericenter distance can be measured with the aLIGO–AdV–KAGRA detector network either if the binary forms in the detectors' frequency band or if it forms not far outside of it such that $e_{10\,\mathrm{Hz}} \gtrsim 0.1$. The errors are in the range $\Delta e_0 \sim (10^{-3} - 10^{-1}) \times (D_L/100\,\mathrm{Mpc})$ and $\Delta \rho_{p0} \sim (0.01 - 10) \times (D_L/100\,\mathrm{Mpc})$, with the smallest errors for binaries that form in the GW detectors' frequency

band near the low-frequency cutoff of the detectors or at $e_{10\,\mathrm{Hz}} \sim e_0$, where errors systematically decrease with $e_{10\,\mathrm{Hz}}$ and weakly depend on the binary mass.

These results are encouraging as they suggest that the upcoming second-generation GW detector network (Abbott et al. 2018) at design sensitivity has the capability to distinguish between eccentric waveforms and circular waveforms, implying that the eccentricity may be used to constrain the astrophysical origin of GW source populations. These may include binary–single or binary–binary encounters in dense stellar systems such as in globular clusters or in active galactic nucleus gaseous disks, single–single GW capture encounters, Kozai–Lidov effect in field triples, or Kozai–Lidov effect caused by a supermassive black hole for binaries in galactic nuclei (see Introduction). However, further work is needed to verify if these conclusions hold when higher post-Newtonian order waveforms or waveforms of numerical relativity simulations, spin effects, perturbations related to tidal deformability, posterior parameter distributions with Monte Carlo Markov chain methods and Bayesian inference, and theoretical errors due to inaccuracies in the waveform model are included. In particular, the errors may be much worse than in our estimates for precessing eccentric NS–BH and BH–BH binaries with high BH masses or in cases where binaries form at small ρ_{p0} because in this case, the detected signal starts at a separation where these corrections are already significant. Indeed, note that the PN expansion parameter approximately satisfies $v^2/c^2 \propto \rho_p^{-1}$, so that $\rho_p \gg 10$ is required for higher-order PN effects to be negligible. Our conclusions may be accurate in cases where these corrections are negligible, when the binary waveform enters the GW detectors' frequency band at relatively high pericenter distance ρ_p. For instance, for initially highly eccentric NS–NS binaries, the binary forms with $f_{\mathrm{GW}} < 10\,\mathrm{Hz}$ at $\rho_{p0} \gtrsim 150$. Similarly, for initially highly eccentric NS–BH binaries with relatively low BH masses below $\sim 20\,M_\odot$, the initial pericenter is $\rho_{p0} \gtrsim 40$ if the binary forms with $f_{\mathrm{GW}} < 10\,\mathrm{Hz}$. In these cases, the 1PN results may be expected to be relatively accurate.

We conclude that further development of GW data analysis algorithms to detect eccentric inspiraling GW sources and to measure their physical parameters may offer high rewards in GW astronomy for interpreting the astrophysical origin of GW sources.

Appendix A
Residual Eccentricity as a Function of Waveform Parameters

In this section, we express $e_{10\,\mathrm{Hz}}$ as a function of e_{LSO} and M_{tot}. Based on Peters (1964), we showed in Gondán et al. (2018a) that the product $\nu(e)H(e)$ is conserved during the

---

[19] I.e., when GWs start to drive the inspiral of the binary and dominate the evolution, such as after a binary-forming close encounter of single–single objects due to GW losses, or after a binary–single or binary–binary encounter that places the binary on an inspiraling trajectory.

evolution of the binary, where $H(e)$ is defined as

$$H(e) = e^{18/19}(1-e^2)^{-3/2}\left(1 + \frac{121}{304}e^2\right)^{\frac{1305}{2299}}, \qquad (18)$$

and $\nu(e)$ is the redshifted Keplerian mean orbital frequency:

$$\nu(e, \rho_{\rm p}) = \frac{(1-e)^{3/2}}{2\pi M_{\rm tot}\rho_{\rm p}^{3/2}(e)}. \qquad (19)$$

Here, we use the leading-order orbital evolution equation (Peters 1964)

$$\rho_{\rm p}(e) = \frac{c_0}{M_{\rm tot}}\frac{e^{12/19}}{(1+e)}\left(1 + \frac{121}{304}e^2\right)^{\frac{870}{2299}}, \qquad (20)$$

where $c_0/M_{\rm tot}$ may be expressed with e_0 and $\rho_{\rm p0}$ by solving Equation (20) for $\rho_{\rm p} = \rho_{\rm p0}$ and $e = e_0$. Here, $\nu(e)H(e) \equiv$ const for $e_{\rm LSO} \leqslant e \leqslant e_0$. Thus, $e_{10\,\rm Hz}$ may be expressed with either e_0 or $e_{\rm LSO}$.

Here, we write out the expressions for $e_{\rm LSO}$. By setting

$$\nu(e_{10\,\rm Hz})H(e_{10\,\rm Hz}) = \nu(e_{\rm LSO})H(e_{\rm LSO}) \qquad (21)$$

and substituting $\nu(e)$ with Equation (19) in Equation (21). This leads to the following implicit equation for $e_{10\,\rm Hz}$:

$$\frac{(1-e_{10\,\rm Hz})^{3/2}H(e_{10\,\rm Hz})}{\rho_{10\,\rm Hz}^{3/2}} = \frac{(1-e_{\rm LSO})^{3/2}H(e_{\rm LSO})}{\rho_{\rm p,LSO}^{3/2}}. \qquad (22)$$

Here, $\rho_{10\,\rm Hz}$ is defined by rewriting Equation (8) at $e = e_{10\,\rm Hz}$ as

$$\rho_{10\,\rm Hz} = ((1+e_{10\,\rm Hz})^{0.3046}\pi M_{\rm tot,z}f_{\rm det})^{-2/3}, \qquad (23)$$

where $f_{\rm det} = 10$ Hz (Section 2.8). In Equation (22), we define $\rho_{\rm LSO}$ for eccentric BH–BH binaries as $\rho_{\rm p,LSO} = (6 + 2e_{\rm LSO})/(1 + e_{\rm LSO})$, and for eccentric NS–NS and NS–BH binaries as 8.5 and 7.5, respectively; see Section 2.2 for details. After combining Equation (22) with Equation (23), we obtain a result of the form $e_{10\,\rm Hz} \equiv e_{10\,\rm Hz}(e_{\rm LSO}, M_{\rm tot,z})$. A similar derivation gives $e_{10\,\rm Hz} \equiv e_{10\,\rm Hz}(e_0, M_{\rm tot,z})$ when e_0 is set instead of $e_{\rm LSO}$ in Equation (21). We tested the algorithms numerically to ensure that both $e_{10\,\rm Hz}$ and $\Delta e_{10\,\rm Hz}$ are correctly calculated.

Appendix B
The Total Signal-to-noise Ratio and Parameter Measurement Errors as a Function of D_L

In this section, we determine numerically how the S/N$_{\rm tot}$ and the parameter measurement errors scale with D_L in order to scale our $D_L = 100$ Mpc results to higher D_L values.

The D_L dependence of the S/N$_{\rm tot}$ and parameter measurement errors may be given by their respective definition.[20] The signal-to-noise ratio and the Fisher matrix elements depend on the spectral GW amplitude, which scales as $1/D_L$. Furthermore, there is a cosmological redshift dependence of mass parameters that varies with distance, i.e., $m_z = (1 + z)m$, where $z = z(D_L)$ according to Equation (6). Here, $z(D_L)$ may be obtained numerically using the inverse function of Equation (6).

If D_L is relatively small such that $z \ll 1$, the S/N$_{\rm tot}$ and parameter measurement errors scale as $\propto 1/D_L$ and $\propto D_L$,

respectively. However, for higher D_L, the z dependence becomes significant, which modifies the distance dependence. The S/N$_{\rm tot}$ and the components of the Fisher matrix have a non-monotonic $M_{\rm tot,z}$ dependence for the considered waveform model.[21]

We determine S/N$_{\rm tot}$ and parameter measurement errors numerically as in Section 2.7, but now vary D_L instead of $\rho_{\rm p0}$. We present scaling relations for these quantities between 100 Mpc and 1 Gpc, where the numerical algorithms have been validated.

We find that the S/N$_{\rm tot}$ is best fit with a power-law profile $\propto D_L^{-\gamma}$, where $\gamma \approx 1.03$–1.07 depending on the component masses and $\rho_{\rm p0}$. Similarly, measurement errors of binary parameters can also be approximated as $\propto D_L^{\kappa}$, where $\kappa \approx 1.02$–1.1 depending on the component masses, $\rho_{\rm p0}$, and the parameter. Using $\gamma = 1$ leads to inaccuracies at the level of 5%–12% and 7%–17% for $D_L = 500$ Mpc and 1 Gpc, respectively, for the S/N$_{\rm tot}$. Similarly for the measurement errors of binary parameters, these inaccuracies are at the level of 3%–15% and 5%–21% for the same D_L values when $\kappa = 1$ is used.

ORCID iDs

László Gondán ● https://orcid.org/0000-0003-0685-7518
Bence Kocsis ● https://orcid.org/0000-0002-4865-7517

References

Aasi, J., Abadie, J., Abbott, B. P., et al. 2015, CQGra, 32, 115012
Abadie, J., Abbott, B. P., Abbott, R., et al. 2010, CQGra, 27, 173001
Abbott, B. P., Abbott, R., Abbott, T. D., et al. 2016a, PhRvX, 6, 041015
Abbott, B. P., Abbott, R., Abbott, T. D., et al. 2016b, PhRvL, 116, 241103
Abbott, B. P., Abbott, R., Abbott, T. D., et al. 2016c, PhRvL, 116, 061102
Abbott, B. P., Abbott, R., Abbott, T. D., et al. 2016d, PhRvD, 93, 122004
Abbott, B. P., Abbott, R., Abbott, T. D., et al. 2016e, LRR, 19, 1
Abbott, B. P., Abbott, R., Abbott, T. D., et al. 2016f, PhRvL, 116, 221101
Abbott, B. P., Abbott, R., Abbott, T. D., et al. 2016g, ApJL, 832, L21
Abbott, B. P., Abbott, R., Abbott, T. D., et al. 2017a, PhRvL, 118, 221101
Abbott, B. P., Abbott, R., Abbott, T. D., et al. 2017b, ApJL, 851, L35
Abbott, B. P., Abbott, R., Abbott, T. D., et al. 2017c, PhRvL, 119, 141101
Abbott, B. P., Abbott, R., Abbott, T. D., et al. 2017d, PhRvL, 119, 161101
Abbott, B. P., Abbott, R., Abbott, T. D., et al. 2018, LRR, 21, 3
Acernese, F., Agathos, M., Agatsuma, K., et al. 2015, CQGra, 32, 024001
Ajith, P., & Bose, S. 2009, PhRvD, 79, 084032
Alsing, J., Silva, H. O., & Berti, E. 2018, MNRAS, 478, 1377
Antognini, J. M., Shappee, B. J., Thompson, T. A., & Amaro-Seoane, P. 2014, MNRAS, 439, 1079
Antoniadis, J., Tauris, T. M., Ozel, F., et al. 2016, arXiv:1605.01665
Antonini, F., & Perets, H. B. 2012, ApJ, 757, 27
Antonini, F., & Rasio, F. A. 2016, ApJ, 831, 187
Antonini, F., Toonen, S., & Hamers, A. S. 2017, ApJ, 841, 77
Antonini, R., Rodriguez, C. L., Petrovich, C., & Fischer, C. L. 2018, MNRAS, 480, 4
Arca Sedda, M., & Benacquista, M. 2019, MNRAS, 482, 2991
Arca-Sedda, M., Li, G., & Kocsis, B. 2018, arXiv:1805.06458
Arun, K. G., Iyer, B. R., Sathyaprakash, B. S., & Sundararajan, P. A. 2005, PhRvD, 71, 084008
Bai, Y., Barger, V., & Lu, S. 2018, arXiv:1802.04909
Bailyn, C. D., Jain, R. K., Coppi, P., & Orosz, J. A. 1998, ApJ, 499, 367
Baiotti, L., & Rezzolla, L. 2017, RPPh, 80, 096901
Barack, L., Cardoso, V., Nissanke, S., et al. 2018, arXiv:1806.05195
Bauswein, A., Ardevol Pulpillo, R., Janka, H.-T., & Goriely, S. 2014, ApJL, 795, L9
Belczynski, K., Buonanno, A., Cantiello, M., et al. 2014, ApJ, 789, 120
Belczynski, K., Heger, A., Gladysz, W., et al. 2016b, A&A, 594, A97

Belczynski, K., Repetto, S., Holz, D. E., et al. 2016a, ApJ, 819, 108
Belczynski, K., Wiktorowicz, G., Fryer, C. L., Holz, D. E., & Kalogera, V. 2012, ApJ, 757, 91
Berger, E. 2014, ARA&A, 52, 43
Berry, C. P. L., Mandel, I., Middleton, H., et al. 2015, ApJ, 804, 114
Berti, E., Cardoso, V., Hinderer, T., et al. 2010, PhRvD, 81, 104048
Biwer, C. M., Capano, C. D., De, S., et al. 2019, PASP, 131, 024503
Blanchet, L. 2014, LRR, 17, 2
Breivik, K., Rodriguez, C. L., Larson, S. L., Kalogera, V., & Rasio, F. A. 2016, ApJL, 830, L18
Brown, D. A., & Zimmerman, P. J. 2010, PhRvD, 81, 024007
Canizares, P., Field, S. E., Gair, J., et al. 2015, PhRvL, 114, 071104
Cannon, K., Cariou, R., Chapman, A., et al. 2012, ApJ, 748, 136
Chatziioannou, K., Cornish, N., Klein, A., & Yunes, N. 2014, PhRvD, 89, 104023
Cho, H.-S., Ochsner, E., O'Shaughnessy, R., Kim, C., & Lee, C.-H. 2013, PhRvD, 87, 024004
Cholis, I., Kovetz, E. D., Ali-Haïmoud, Y., et al. 2016, PhRvD, 94, 084013
Christian, P., Mocz, P., & Loeb, A. 2018, ApJL, 858, L8
Chruslinska, M., Belczynski, K., Klencki, J., & Benacquista, M. 2018, MNRAS, 474, 2937
Cornish, N. J., & Littenberg, T. B. 2015, CQGra, 32, 135012
Coughlin, M., Meyers, P., Thrane, E., Luo, J., & Christensen, N. 2015, PhRvD, 91, 063004
Coughlin, M. W., Dietrich, T., Margalit, B., & Metzger, B. D. 2018, arXiv:1812.04803
Coward, D. M., Howell, E. J., Piran, T., et al. 2012, MNRAS, 425, 2668
Cutler, C., & Flanagan, É. E. 1994, PhRvD, 49, 2658
Cutler, C., Kennefick, D., & Poisson, E. 1994, PhRvD, 50, 3816
D'Orazio, D. J., & Samsing, J. 2018, MNRAS, 481, 4775
Davis, M., Ruffini, R., Tiomno, J., & Zerilli, F. 1972, PhRvL, 28, 1352
de Mink, S. E., & Belczynski, K. 2015, ApJ, 814, 58
Dietrich, T., Moldenhauer, N., Johnson-McDaniel, N. K., et al. 2015, PhRvD, 92, 124007
Dominik, M., Berti, E., O'Shaughnessy, R., et al. 2015, ApJ, 806, 263
Dudi, R., Pannarale, F., Dietrich, T., et al. 2018, PhRvD, 98, 084061
East, W. E., McWilliams, S. T., Levin, J., & Pretorius, F. 2013, PhRvD, 87, 043004
East, W. E., Paschalidis, V., & Pretorius, F. 2015, ApJL, 807, L3
East, W. E., Paschalidis, V., Pretorius, F., & Shapiro, S. L. 2016, PhRvD, 93, 024011
East, W. E., & Pretorius, F. 2012, ApJL, 760, L4
East, W. E., Pretorius, F., & Stephens, B. C. 2012, PhRvD, 85, 124009
Faber, J. A., & Rasio, F. A. 2012, LRR, 15, 8
Fabian, A. C., Pringle, J. E., & Rees, M. J. 1975, MNRAS, 172, 15p
Fan, X., Li, J., Li, X., Zhong, Y., & Cao, J. 2018, arXiv:1811.01380
Farr, B., Berry, C. P. L., Farr, W. M., et al. 2016, ApJ, 825, 116
Farr, B., Holz, D. E., & Farr, W. M. 2018, ApJL, 854, L9
Farr, W. M., Sravan, N., Cantrell, A., et al. 2011, ApJ, 741, 103
Farr, W. M., Stevenson, S., Miller, M. C., et al. 2017, Natur, 548, 426
Favata, M. 2014, PhRvL, 112, 101101
Fishbach, M., & Holz, D. E. 2017, ApJL, 851, L25
Fishbach, M., Holz, D. E., & Farr, B. 2017, ApJL, 840, L24
Fong, W., Berger, E., Margutti, R., & Zauderer, B. A. 2015, ApJ, 815, 102
Fragione, G., Grishin, E., Leigh, N. W. C., Perets, H. B., & Perna, R. 2018, arXiv:1811.10627
Gerosa, D., Berti, E., O'Shaughnessy, R., et al. 2018, PhRvD, 98, 084036
Giacobbo, N., Mapelli, M., & Spera, M. 2018, MNRAS, 474, 2959
Gilmer, M. S., Kozyreva, A., Hirschi, R., Fröhlich, C., & Yusof, N. 2017, ApJ, 846, 100
Gold, R., Bernuzzi, S., Thierfelder, M., Brügmann, B., & Pretorius, F. 2012, PhRvD, 86, 121501
Gondán, L., Kocsis, B., Raffai, P., & Frei, Z. 2018a, ApJ, 855, 34
Gondán, L., Kocsis, B., Raffai, P., & Frei, Z. 2018b, ApJ, 860, 5
Grindlay, J., Portegies Zwart, S., & McMillan, S. 2006, NatPh, 2, 116
Harry, I., & Hinderer, T. 2018, CQGra, 35, 145010
Healy, J., Ruchlin, I., Lousto, C. O., & Zlochower, Y. 2016, PhRvD, 94, 104020
Huerta, E. A., & Brown, D. A. 2013, PhRvD, 87, 127501
Huerta, E. A., Kumar, P., Agarwal, B., et al. 2017, PhRvD, 95, 024038
Huerta, E. A., Kumar, P., McWilliams, S. T., O'Shaughnessy, R., & Yunes, N. 2014, PhRvD, 90, 084016
Huerta, E. A., Moore, C. J., Kumar, P., et al. 2018, PhRvD, 97, 024031
Inayoshi, K., Tamanini, N., Caprini, C., & Haiman, Z. 2017, PhRvD, 96, 063014
Iyer, B., IndIGO, LIGO Scientfic Collaboration, et al. 2011, LIGO, Tech. Rep. LIGO-M1100296-v2

Jin, Z.-P., Li, X., Cano, Z., et al. 2015, ApJL, 811, L22
Kalogera, V., Kim, C., Lorimer, D. R., et al. 2004, ApJL, 601, L179
Kim, C., Perera, B. B. P., & McLaughlin, M. A. 2015, MNRAS, 448, 928
Kiziltan, B., Kottas, A., De Yoreo, M., & Thorsett, S. E. 2013, ApJ, 778, 66
Klimenko, S., Vedovato, G., Drago, M., et al. 2016, PhRvD, 93, 042004
Kocsis, B., Gáspár, M. E., & Márka, S. 2006, ApJ, 648, 411
Kocsis, B., Haiman, Z., Menou, K., & Frei, Z. 2007, PhRvD, 76, 022003
Kocsis, B., & Levin, J. 2012, PhRvD, 85, 123005
Kowalska, I., Bulik, T., Belczynski, K., Dominik, M., & Gondek-Rosinska, D. 2011, A&A, 527, A70
Kremer, K., Chatterjee, S., Breivik, K., et al. 2018, PhRvL, 120, 191103
Kruckow, M. U., Tauris, T. M., Langer, N., Kramer, M., & Izzard, R. G. 2018, MNRAS, 481, 1908
Kyutoku, K., & Seto, N. 2014, MNRAS, 441, 1934
Lang, R. N., & Hughes, S. A. 2006, PhRvD, 74, 122001
Lee, W. H., Ramirez-Ruiz, E., & van de Ven, G. 2010, ApJ, 720, 953
Littenberg, T. B., & Cornish, N. J. 2015, PhRvD, 91, 084034
Liu, B., & Lai, D. 2017, ApJL, 846, L11
Liu, B., & Lai, D. 2018, ApJ, 863, 68
Lopez, M., Jr., Batta, A., Ramirez-Ruiz, E., Martinez, I., & Samsing, J. 2018, arXiv:1812.01118
Loutrel, N., Yunes, N., & Pretorius, F. 2014, PhRvD, 90, 104010
Lower, M. E., Thrane, E., Lasky, P. D., & Smith, R. 2018, PhRvD, 98, 083028
Ma, S., Cao, Z., Lin, C.-Y., Pan, H.-P., & Yo, H.-J. 2017, PhRvD, 96, 084046
Mandel, I., Farr, W. M., Colonna, A., et al. 2017, MNRAS, 465, 3254
Mapelli, M., Giacobbo, N., Ripamonti, E., & Spera, M. 2017, MNRAS, 472, 2422
Marchant, P., Langer, N., Podsiadlowski, P., Tauris, T. M., & Moriya, T. J. 2016, A&A, 588, A50
Margalit, B., & Metzger, B. D. 2017, ApJL, 850, L19
Meiron, Y., Kocsis, B., & Loeb, A. 2017, ApJ, 834, 200
Mikóczi, B., Kocsis, B., Forgács, P., & Vasúth, M. 2012, PhRvD, 86, 104027
Miller, B., O'Shaughnessy, R., Littenberg, T. B., & Farr, B. 2015, PhRvD, 92, 044056
Millhouse, M., Cornish, N. J., & Littenberg, T. 2018, PhRvD, 97, 104057
Moreno-Garrido, C., Buitrago, J., & Mediavilla, E. 1994, MNRAS, 266, 16
Moreno-Garrido, C., Mediavilla, E., & Buitrago, J. 1995, MNRAS, 274, 115
Ng, K. K. Y., Vitale, S., Zimmerman, A., et al. 2018, PhRvD, 98, 083007
Nicholson, D., & Vecchio, A. 1998, PhRvD, 57, 4588
Nishizawa, A., Berti, E., Klein, A., & Sesana, A. 2016, PhRvD, 94, 064020
Nishizawa, A., Sesana, A., Berti, E., & Klein, A. 2017, MNRAS, 465, 4375
Nissanke, S., Holz, D. E., Hughes, S. A., Dalal, N., & Sievers, J. L. 2010, ApJ, 725, 496
O'Leary, R. M., Kocsis, B., & Loeb, A. 2009, MNRAS, 395, 2127
O'Leary, R. M., Meiron, Y., & Kocsis, B. 2016, ApJL, 824, L12
O'Shaughnessy, R., Farr, B., Ochsner, E., et al. 2014, PhRvD, 89, 102005
Özel, F., & Freire, P. 2016, ARA&A, 54, 401
Özel, F., Psaltis, D., Narayan, R., & McClintock, J. E. 2010, ApJ, 725, 1918
Özel, F., Psaltis, D., Narayan, R., & Santos Villarreal, A. 2012, ApJ, 757, 55
Papenfort, L. J., Gold, R., & Rezzolla, L. 2018, PhRvD, 98, 104028
Paschalidis, V., East, W. E., Pretorius, F., & Shapiro, S. L. 2015, PhRvD, 92, 121502
Paschalidis, V., & Stergioulas, N. 2017, LRR, 20, 7
Peters, P. C. 1964, PhRv, 136, 1224
Petrillo, C. E., Dietz, A., & Cavaglià, M. 2013, ApJ, 767, 140
Petrovich, C., & Antonini, F. 2017, ApJ, 846, 146
Piran, T., Nakar, E., & Rosswog, S. 2013, MNRAS, 430, 2121
Planck Collaboration, Ade, P. A. R., Aghanim, N., et al. 2014a, A&A, 571, A1
Planck Collaboration, Ade, P. A. R., Aghanim, N., et al. 2014b, A&A, 571, A16
Poisson, E., & Will, C. M. 1995, PhRvD, 52, 848
Pooley, D., Lewin, W. H. G., Anderson, S. F., et al. 2003, ApJL, 591, L131
Privitera, S., Mohapatra, S. R. P., Ajith, P., et al. 2014, PhRvD, 89, 024003
Radice, D., Galeazzi, F., Lippuner, J., et al. 2016, MNRAS, 460, 3255
Ramirez-Ruiz, E., Trenti, M., MacLeod, M., et al. 2015, ApJL, 802, L22
Randall, L., & Xianyu, Z.-Z. 2018a, ApJ, 864, 134
Randall, L., & Xianyu, Z.-Z. 2018b, ApJ, 853, 93
Rodriguez, C. L., Amaro-Seoane, P., Chatterjee, S., et al. 2018a, arXiv:1811.04926
Rodriguez, C. L., Amaro-Seoane, P., Chatterjee, S., & Rasio, F. A. 2018b, PhRvL, 120, 151101
Rodriguez, C. L., Farr, B., Raymond, V., et al. 2014, ApJ, 784, 119
Rodriguez, C. L., Zevin, M., Pankow, C., Kalogera, V., & Rasio, F. A. 2016, ApJL, 832, L2
Rosswog, S., Piran, T., & Nakar, E. 2013, MNRAS, 430, 2585

Samsing, J. 2018, PhRvD, 97, 103014
Samsing, J., & D'Orazio, D. J. 2018, MNRAS, 481, 5445
Samsing, J., D'Orazio, D. J., Askar, A., & Giersz, M. 2018, arXiv:1802.08654
Samsing, J., MacLeod, M., & Ramirez-Ruiz, E. 2014, ApJ, 784, 71
Samsing, J., & Ramirez-Ruiz, E. 2017, ApJL, 840, L14
Schrøder, S. L., Batta, A., & Ramirez-Ruiz, E. 2018, ApJL, 862, L3
Seto, N. 2013, PhRvL, 111, 061106
Shappee, B. J., & Thompson, T. A. 2013, ApJ, 766, 64
Siellez, K., Boër, M., & Gendre, B. 2014, MNRAS, 437, 649
Silsbee, K., & Tremaine, S. 2017, ApJ, 836, 39
Singer, L. P., & Price, L. R. 2016, PhRvD, 93, 024013
Somiya, K. 2012, CQGra, 29, 124007
Stephens, B. C., East, W. E., & Pretorius, F. 2011, ApJL, 737, L5
Stevenson, S., Berry, C. P. L., & Mandel, I. 2017, MNRAS, 471, 2801
Stevenson, S., Ohme, F., & Fairhurst, S. 2015, ApJ, 810, 58
Sun, B., Cao, Z., Wang, Y., & Yeh, H.-C. 2015, PhRvD, 92, 044034
Tai, K. S., McWilliams, S. T., & Pretorius, F. 2014, PhRvD, 90, 103001
Talbot, C., & Thrane, E. 2017, PhRvD, 96, 023012
The LIGO Scientific Collaboration & the Virgo Collaboration, 2018, arXiv:1811.12907
Thompson, T. A. 2011, ApJ, 741, 82

Tiwari, V., Klimenko, S., Christensen, N., et al. 2016, PhRvD, 93, 043007
Tsang, D. 2013, ApJ, 777, 103
Unnikrishnan, C. S. 2013, IJMPD, 22, 1341010
Valentim, R., Rangel, E., & Horvath, J. E. 2011, MNRAS, 414, 1427
Vangioni, E., Goriely, S., Daigne, F., François, P., & Belczynski, K. 2016, MNRAS, 455, 17
Veitch, J., Raymond, V., Farr, B., et al. 2015, PhRvD, 91, 042003
Vigna-Gómez, A., Neijssel, C. J., Stevenson, S., et al. 2018, MNRAS, 481, 4009
Vinciguerra, S., Veitch, J., & Mandel, I. 2017, CQGra, 34, 115006
Vitale, S., Lynch, R., Sturani, R., & Graff, P. 2017, CQGra, 34, 03LT01
Vivekanandji Chaurasia, S., Dietrich, T., Johnson-McDaniel, N. K., et al. 2018, arXiv:1807.06857
Wen, L. 2003, ApJ, 598, 419
Woosley, S. E. 2017, ApJ, 836, 244
Yunes, N., Arun, K. G., Berti, E., & Will, C. M. 2009, PhRvD, 80, 084001
Zaldarriaga, M., Kushnir, D., & Kollmeier, J. A. 2018, MNRAS, 473, 4174
Zevin, M., Pankow, C., Rodriguez, C. L., et al. 2017, ApJ, 846, 82
Zevin, M., Samsing, J., Rodriguez, C., Haster, C.-J., & Ramirez-Ruiz, E. 2018, arXiv:1810.00901
Zhao, W., & Wen, L. 2018, PhRvD, 97, 064031